machines

MDPI

Article

NDF Controller-Based Stability Analysis and Vibration Mitigation of a Nonlinear Electromechanical Oscillator Under Primary Resonance

Ashraf Taha EL-Sayed [1,*], Rageh K. Hussein [2], Yasser A. Amer [3], Fatma Sherif Mohammed [4], Sharif Abu Alrub [2] and Taher A. Bahnasy [5]

[1] Department of Basic Science, Modern Academy for Engineering and Technology, Elmokattam, Cairo 11439, Egypt
[2] Physics Department, College of Science, Imam Mohammad Ibn Saud Islamic University (IMSIU), Riyadh 11623, Saudi Arabia; rahussein@imamu.edu.sa (R.K.H.); snabualrub@imamu.edu.sa (S.A.A.)
[3] Department of Mathematics, Faculty of Science, Zagazig University, Zagazig 44759, Egypt; yaamer@zu.edu.eg
[4] Faculty of Engineering, Egypt University of Informatics, New Administrative Capital, Cairo 19519, Egypt; fatma.mohamed@eui.edu.eg or f.sheref22@science.zu.edu.eg
[5] Department of Physics and Engineering Mathematics, Faculty of Engineering, Tanta University, Tanta 31734, Egypt; taher.bahnasy@f-eng.tanta.edu.eg
* Correspondence: ashraftaha211@yahoo.com or atelsayed@eng.modern-academy.edu.eg

Abstract

This work examines how well a Negative Derivative Feedback (NDF) controller suppresses vibration in a nonlinear electromechanical oscillator that is subjected to mixed excitations. Coupled nonlinear ordinary differential equations are used to model the system and show how mechanical and electrical components interact. The method of multiple scales (MMS) is used to develop analytical approximate solutions up to the second order, specifically for the primary resonance scenario. This study's main contribution is a thorough bifurcation analysis and proof of the NDF controller's high efficacy, which effectively lowers the first and second mode resonance amplitudes by roughly 99.8% and 98%., respectively, with impressive reported effectiveness values of roughly 590 and 51.5. Additionally, the quantitative error analysis between the numerical simulation and the analytical approximation solution demonstrates a high degree of agreement, with a maximum error of less than 10^{-5}% for the second mode and just 0.01% for the first mode. Furthermore, we present the impact of parameters on FRCs. Frequency response curves (FRCs) are used in a thorough comparison analysis to assess the behavior of the system both before and after the controller is activated. A strong degree of connection between the analytical conclusions and numerical simulations carried out using the "fourth-order Runge–Kutta method" rigorously validates the accuracy of the perturbation analysis. Additionally, a performance benchmark between different control techniques, such as the NDF controller, Positive Position Feedback (PPF), and Linear Negative Position Feedback (LNPF), is shown in the paper. When compared to alternative approaches, the NDF controller shows the greatest reduction in oscillation amplitudes and higher robustness, as shown by transient response analysis (time history) at various time intervals. The outcomes validate the NDF approach's dependability and efficiency in stabilizing intricate nonlinear electromechanical systems. The chaotic response and system periodicity were demonstrated through bifurcation diagrams and Poincaré maps.

Keywords: electromechanical system; MMS; NDF; vibration control; time history; FRCs; stability

Check for updates

Academic Editor: Zheng Chen

Received: 21 May 2026
Revised: 17 June 2026
Accepted: 21 June 2026
Published: 24 June 2026

Copyright: © 2026 by the authors. Licensee MDPI, Basel, Switzerland. This article is an open access article distributed under the terms and conditions of the Creative Commons Attribution (CC BY) license.

1. Introduction

In order to develop the future of micro- and nano-electromechanical systems (MEMS/NEMS), it is essential to be able to control the nonlinear coupling between vibrational modes. These linked oscillators provide essential frameworks for deciphering intricate dynamics in a variety of biological, engineering, and physical schemes. In general, high precision applications, including thickness measurement, rotational speed computation, and flow identification in materials ranging from steel to sophisticated alloys, are carried out using electromagnetic transducers. The mechanical part serves as the main sensor in these system, while the electrical subsystem uses magnetic interaction to send vibration signals through the air gap of a permanent magnet; this creates a special synergy [1]. Several important works have thoroughly examined the area of nonlinear electromechanical system. Yamapi et al. [2] investigated the chaotic management mechanism and stability feature of these system. Ge and Lin [3] used adaptive and delayed feedback control approaches to study the dynamic behavior of electromechanical gyrostat systems exposed to external disturbance.Yamapi and Bowong [4] used sliding mode controllers to a control self-sustaining electrostatic transducer system while taking discontinuous and continuous states into account. In terms of geophysical applications, Siewe et al. [5] created an electromechanical oscillator to capture the earth's vertical motion, proving that the accuracy of the damping coefficient estimation is a crucial factor in the efficacy of chaos suppression. Subsequent research [6,7] used the averaging and harmonic balance methods to evaluate the synchronization between coupled systems, such as Rayliegh–Duffing oscillators, in order to calculate oscillatory amplitudes. Furthermore, a thorough examination of global bifurcations and the complex dynamics of self-sustained nonlinear electromechanical system was conducted by Kwuimy and Woafo [8,9].

Hegazy [10] examined nonlinear vibrations and chaotic motions in an electromechanical seismograph system with time-varying stiffness. He employed various active controller types to lessen system oscillations and discovered that the most effective active control on system behavior is negative velocity feedback. Recently, the behavior of electromechanical schemes and how they affect the energy harvesting problem have drawn the attention of researchers. Martens et al. [11] examined the efficiency of vibration energy harvesting systems affected by sporadic environmental excitations using the solution of applicable Fokker–Planck formulas. Borowiec et al. [12] examined the effects of random excitation on energy harvester performance and showed that the noise component of the force impacts the stability of the system. In order to assess a nonlinear energy harvesting system's mean square electric voltage, a stochastic averaging technique was presented in [13]. Li et al. [14] investigated a piezoelectric energy harvester with external magnetic fields driving tri-stable potential wells. They asserted that if the system is properly constructed, the frequency bandwidth can be increased for this high harvesting efficiency at coherence resonance with a certain deterministic or stochastic input. Additionally, Pallay et al. [15] looked into the basic processes of control phase deviations in semi-active systems and suggested a structure-based compensation strategy that uses inertial suspensions to remove phase delays across the whole frequency range.

Averaging techniques and the multiple scales method (MSM) [16–18] are two perturbation methods frequently used to evaluate the effectiveness of parametrically stimulated models. The behavior of such systems can still be predicted using these techniques, particularly in the frequency region near the important parametric resonance [19]. In relatively simple circumstances, such as constrained frequency ranges around the core parametric resonance, modest excitations, and minimum system properties, it has been demonstrated that traditional MSM can accurately estimate responses [20–23]. Furthermore, it has been

demonstrated that a number of control mechanism techniques can lessen the harmful vibrations that various nonlinear systems create [24–31].

Elsayed et al. [32] examined how well a Negative Derivative Feedback (NDF) controller suppressed vibrations in a nonlinear system with two degrees of freedom and geometric damping. They thoroughly examined the system's behavior under simultaneous resonance conditions by using the averaging method in conjunction with Runge–Kutta numerical simulations. Their findings emphasize the controller's strong ability to improve vibration. A cubic–quintic hybrid oscillator under simultaneous internal and exterior resonances was examined in [33]. The Positive Position Feedback (PPF) controller was found to be the most successful for vibration reduction after a variety of control schemes were assessed. Numerical simulations were used to verify the system's stability after it was further examined utilizing the multiple scale perturbation technique. Hamed et al. [34] investigated the nonlinear dynamics and vibration suppression of a coupled electromechanical oscillator under harmonic and parametric excitations. In [35], to reduce vibrations and stabilize bifurcations in electromechanical systems, this research suggests a unique Nonlinear Proportional-Derivative Cubic Velocity Feedback (NPDVF) controller.

The structural stability and active vibration management of coupled multiphysics setups have drawn a lot of interest in recent research. In particular, Kevorkian and Cole [36] gave a thorough, high-level overview of the most recent developments in nonlinear dynamics as they relate to intricate electromechanical systems. Their study examined the internal energy transfers between mechanical modes and electrical components in detail, highlighting the difficulties caused by undesired large-amplitude resonance in sophisticated energy harvesters, high-precision automobile sensors, and MEMS. Concurrently, Xu et al. [37] carried out a thorough parametric study on the Negative Derivative Feedback (NDF) controller structure in order to lessen these severe dynamic instabilities. They demonstrated the superior effectiveness of the NDF loop in suppressing nonlinear self-excited oscillations without disturbing secondary frequencies by putting forth strong tuning criteria and optimization strategies to maximize its active damping capabilities. While the NDF control system has been studied for structural applications, as see in [38], its application in this work is very different. Here, a two-degree-of-freedom nonlinear electromechanical oscillator is coupled to the NDF controller concurrently. This goes beyond the previously published single-domain models by introducing extremely intricate internal energy interactions between the electrical circuit and mechanical modes under primary resonance.

In this study, two coupled second-order ordinary differential equations with quadratic and cubic nonlinearities are used to describe a nonlinear electromechanical system. Second-order approximate solutions are obtained under the primary resonance condition using the method of multiple scales. Three alternative control systems were compared in order to improve system stability, and the Negative Derivative Feedback (NDF) controller was found to be the most successful. The findings show that the NDF controller greatly reduces vibrations; for the first and second modes, the response amplitude is reduced by 99.8% and 98%, respectively. Additionally, a detailed analysis of the frequency response and the impact of different system factors was conducted. The quantitative error analysis between the numerical simulation and the analytical approximation solution demonstrates a high degree of agreement, with a maximum error of less than 10^{-5}% for the second mode and just 0.01% for the first mode, demonstrating the robustness and dependability of the suggested control strategy. The chaotic response and system periodicity were demonstrated through bifurcation diagrams and Poincaré maps and the optimum parameter selection was made through the system parameter effect graphs and the stability mapping diagrams.

2. Governing Equations and Approximate Solutions

2.1. System Without Control

The scheme of the electromechanical oscillator system under investigation is displayed in Figure 1. The two components of electromechanical device modeling are mechanical and electrical. The electrical component is made up of voltage-charge q, linear inductor L, linear capacitor c, and linear resistor R. The mechanical component is made up of a big suspended object. A radial magnetic field is produced when the mechanical and electrical components interact via a permanent magnet's air gap.

The equation of motion of a 2-DOF electromechanical system and its schematic configuration (Figure 1) are adopted from [34,35] as follows:

$$\ddot{x} + \varepsilon\mu_1\dot{x} + \omega_1^2 x + \varepsilon\lambda_1 x^2 + \varepsilon\lambda_2 x^3 + \varepsilon(\gamma_0 + \gamma_1 x + \gamma_2 x^2)\dot{y} = \varepsilon(f_0 + f_1\cos(\Omega_1 t) + f_2 x\cos(\Omega_2 t)) \quad (1)$$

$$\ddot{y} + \varepsilon\mu_2\dot{y} + \omega_2^2 y + \varepsilon(\beta_0 + \beta_1 x + \beta_2 x^2)\dot{x} = \varepsilon(f_3\cos(\Omega_3 t) + f_4 y\cos(\Omega_4 t)) \quad (2)$$

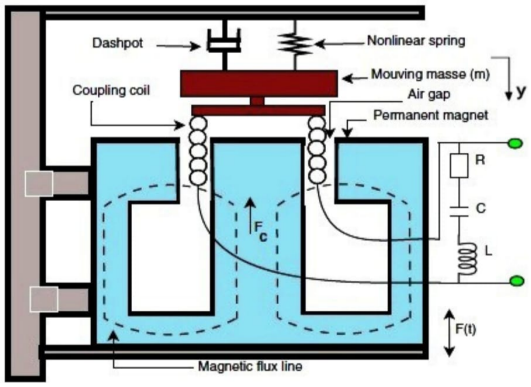

Figure 1. A schematic of an electromechanical seismograph model featuring its integrated electrical circuit.

Two coupled components make up the system: an electrical part represented by a linear damped oscillator with nonlinear coupling terms (y) and a mechanical part described as a forced Duffing oscillator with nonlinear coupling (x). In this case, the first- and second-order time derivatives with respect to t are denoted by $\dot{x}, \dot{y}$ and $\ddot{x}, \ddot{y}$. The linear damping coefficients and nonlinear parameters are represented by the parameters μ_1, μ_2 and λ_1, λ_2, respectively, whereas ϵ is a minor perturbation parameter ($0 < \epsilon \ll 1$). The excitation force amplitudes are represented by f_i, where mixed mechanical excitations are represented by f_1, f_2, and f_3 and mixed electrical excitations by f_4, f_5. The coupling coefficients are γ_j and β_j ($j = 0, 1, 2$), while ω_1, ω_2 are the natural frequencies and Ω_j are the excitation frequencies. It is worth noting that a number of real-world physical elements that are frequently utilized in engineering applications are directly represented by the coupled electromechanical model examined in this study. In particular, it simulates the dynamic behavior of vibration-based energy harvesting devices, electromagnetic transducers, and micro-electromechanical system (MEMS) resonators, where mechanical structures are intrinsically linked with electrical circuits.

2.2. System with NDF Controller

The governing equations of motion describing the system under the influence of an NDF controller is expressed as follows:

$$\ddot{x} + \varepsilon\mu_1\dot{x} + \omega_1^2 x + \varepsilon\lambda_1 x^2 + \varepsilon\lambda_2 x^3 + \varepsilon(\gamma_0 + \gamma_1 x + \gamma_2 x^2)\dot{y} = \varepsilon(f_0 + f_1\cos(\Omega_1 t) + f_2 x\cos(\Omega_2 t)) + \varepsilon k_1 \dot{u} \quad (3)$$

$$\ddot{y} + \varepsilon\mu_2\dot{y} + \omega_2^2 y + \varepsilon(\beta_0 + \beta_1 x + \beta_2 x^2)\dot{x} = \varepsilon(f_3\cos(\Omega_3 t) + f_4 y\cos(\Omega_4 t)) + \varepsilon k_2 \dot{v} \quad (4)$$

$$\ddot{u} + \varepsilon\mu_3\dot{u} + \omega_3^2 u = -\varepsilon k_3 \dot{x} \quad (5)$$

$$\ddot{v} + \varepsilon\mu_4\dot{v} + \omega_4^2 v = -\varepsilon k_4 \dot{y} \quad (6)$$

The dynamic governing framework of the proposed Negative Derivative Feedback (NDF) controller coupled to the main system is explicitly defined by Equations (5) and (6). In this case, the internal controller signals are represented by the state variables u and v, which are dynamically connected to the primary electromechanical system in Equations (3) and (4) through the control gains k_1, k_2, k_3, and k_4 in order to attain the intended vibration suppression. A Negative Derivative Feedback (NDF) controller is incorporated into this model to improve vibration suppression. To lessen oscillations and enhance overall stability, the NDF controller implements an active dampening mechanism depending on the rate of change in the system's reaction, as shown in Figure 2.

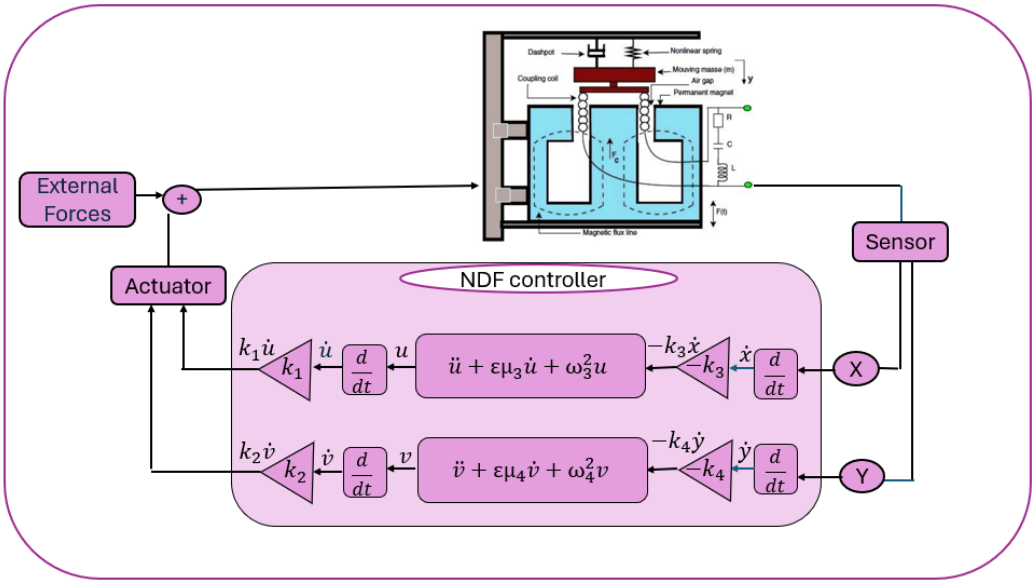

Figure 2. A system model flowchart featuring an NDF controller.

2.3. Perturbation Study

Applying the method of multiple scales by introducing the time scales $T_n = \varepsilon^n t$, the derivatives are transformed as follows [23,35]:

$$\frac{d}{dt} = D_0 + \varepsilon D_1 + \ldots, \quad \frac{d^2}{dt^2} = D_0^2 + 2\varepsilon D_0 D_1 + \ldots \quad (7)$$

We will restrict the study to the first-order approximation

$$x(T_0, T_1, \epsilon) = \sum_{n=0}^{1} \epsilon^n x_n(T_0, T_1) + O(\epsilon^2) \tag{8a}$$

$$y(T_0, T_1, \epsilon) = \sum_{n=0}^{1} \epsilon^n y_n(T_0, T_1) + O(\epsilon^2) \tag{8b}$$

$$u(T_0, T_1, \epsilon) = \sum_{n=0}^{1} \epsilon^n u_n(T_0, T_1) + O(\epsilon^2) \tag{8c}$$

$$v(T_0, T_1, \epsilon) = \sum_{n=0}^{1} \epsilon^n v_n(T_0, T_1) + O(\epsilon^2) \tag{8d}$$

Insert Equations (7) and (8) into Equations (3)–(6) such that:

$$\begin{aligned}(D_0^2 + \omega_1^2)x_0 + (D_0^2 + \omega_1^2)x_1 = \varepsilon\Big[&- 2D_0D_1x_0 - \mu_1 D_0 x_0 - \lambda_1 x_0^2 - \lambda_2 x_0^3 \\ &- \gamma_0 D_0 y_0 - \gamma_1 x_0 D_0 y_0 - \gamma_2 x_0^2 D_0 y_0 + f_0 + f_1\cos(\Omega_1 t) \\ &+ f_2 x_0 \cos(\Omega_2 t) + k_1 D_0 u_0\Big] + O(\varepsilon^2)\end{aligned} \tag{9}$$

$$\begin{aligned}(D_0^2 + \omega_2^2)y_0 + (D_0^2 + \omega_2^2)y_1 = \varepsilon\Big[&- 2D_0D_1y_0 - 2\mu D_0 y_0 - \beta_0 y_0 - \beta_1 x_0 y_0 \\ &- \beta_2 x_0^2 y_0 + f_3\cos(\Omega_3 t) + f_4 y_0 \cos(\Omega_4 t) + k_2 D_0 v_0\Big] + O(\varepsilon^2)\end{aligned} \tag{10}$$

$$(D_0^2 + \omega_3^2)u_0 + (D_0^2 + \omega_3^2)u_1 = \varepsilon\Big[- 2D_0D_1u_0 - \mu_3 D_0 u_0 - k_3 D_0 x_0\Big] + O(\varepsilon^2) \tag{11}$$

$$(D_0^2 + \omega_4^2)v_0 + (D_0^2 + \omega_3^2)v_1 = \varepsilon\Big[- 2D_0D_1v_0 - \mu_4 D_0 v_0 - k_4 D_0 y_0\Big] + O(\varepsilon^2) \tag{12}$$

Collecting the coefficients of order ε^0 and then solving the homogeneous equations yields:

$O(\varepsilon^0)$:

$$(D_0^2 + \omega_1^2)x_0 = 0 \implies x_0 = Ae^{i\omega_1 T_0} + \bar{A}e^{-i\omega_1 T_0} \tag{13a}$$

$$(D_0^2 + \omega_2^2)y_0 = 0 \implies y_0 = Be^{i\omega_2 T_0} + \bar{B}e^{-i\omega_2 T_0} \tag{13b}$$

$$(D_0^2 + \omega_3^2)u_0 = 0 \implies u_0 = Ce^{i\omega_3 T_0} + \bar{C}e^{-i\omega_3 T_0} \tag{13c}$$

$$(D_0^2 + \omega_4^2)v_0 = 0 \implies v_0 = Ee^{i\omega_4 T_0} + \bar{E}e^{-i\omega_4 T_0} \tag{13d}$$

where A, B, C, and E are complex functions in T_1

$O(\varepsilon^1)$:

$$\begin{aligned}(D_0^2 + \omega_1^2)x_1 = &-2D_0D_1x_0 - \mu_1 D_0 x_0 - \lambda_1 x_0^2 - \lambda_2 x_0^3 \\ &- \gamma_0 D_0 y_0 - \gamma_1 x_0 D_0 y_0 - \gamma_2 x_0^2 D_0 y_0 + f_0 + f_1\cos(\Omega_1 t) \\ &+ f_2 x_0 \cos(\Omega_2 t) + k_1 D_0 u_0\end{aligned} \tag{14a}$$

$$\begin{aligned}(D_0^2 + \omega_2^2)y_1 = &-2D_0D_1y_0 - 2\mu D_0 y_0 - (\beta_0 + \beta_1 x_0 + \beta_2 x_0^2)y_0 \\ &+ f_3\cos(\Omega_3 t) + f_4 y_0 \cos(\Omega_4 t) + k_2 D_0 v_0\end{aligned} \tag{14b}$$

$$(D_0^2 + \omega_3^2)u_1 = -2D_0D_1u_0 - \mu_3 D_0 u_0 - k_3 D_0 x_0 \tag{14c}$$

$$(D_0^2 + \omega_4^2)v_1 = -2D_0D_1v_0 - \mu_4 D_0 v_0 - k_4 D_0 y_0 \tag{14d}$$

Substituting Equation (13) into Equation (14) yields:

$$(D_0^2+\omega_1^2)x_1 = \left(-2i\omega_1 D_1 A - i\mu_1\omega_1 A - 3A^2\bar{A}\right)e^{i\omega_1 T_0} - (i\gamma_0\omega_2 B + 2\gamma_2 A\bar{A}B\omega_2)e^{i\omega_2 T_0} - \lambda_2 A^3 e^{3i\omega_1 T_0} - \lambda_1 A^2 e^{2i\omega_1 T_0} - i\gamma_1 AB\omega_2 e^{i(\omega_1+\omega_2)T_0} - i\gamma_1 A\bar{B}\omega_2 e^{i(\omega_1-\omega_2)T_0} - i\gamma_2 A^2 B\omega_2 e^{i(2\omega_1+\omega_2)T_0} + i\gamma_2\bar{B}A^2 e^{i(2\omega_1-\omega_2)T_0} - 2\lambda_1 A\bar{A} + f_0 + \frac{f_1}{2}e^{i\Omega_1 t} + \frac{f_2}{2}Ae^{i(\Omega_2+\omega_1)T_0} + \frac{f_2}{2}Ae^{-i(\Omega_2-\omega_1)T_0} + ik_1 c\omega_3 e^{i\omega_3 T_0} + \text{cc.} \tag{15a}$$

$$(D_0^2+\omega_2^2)y_1 = (-2i\omega_2 D_1 B - i\mu_2\omega_2 B)e^{i\omega_2 T_0} + \frac{f_3}{2}e^{i\Omega_3 t} + \left(-i\beta_0 A\omega_1 - i\beta_2\bar{A}\omega_1\bar{A} + 2i\omega_1 A^2\bar{A}\right)e^{i\omega_1 T_0} + i\beta_2\omega_1 A^3 e^{3i\omega_1 T_0} - i\beta_1 A^2\omega_1 e^{2i\omega_1 T_0} + i\omega_1\beta_1 A\bar{A} + \frac{f_4}{2}Be^{i(\Omega_4+\omega_2)T_0} + \frac{f_4}{2}Be^{-i(\Omega_4-\omega_2)T_0} + ik_2 E\omega_4 e^{i\omega_4 T_0} + \text{cc.} \tag{15b}$$

$$(D_0^2+\omega_3^2)u_1 = (2i\omega_3 D_1 C - i\mu_3\omega_3 C)e^{i\omega_3 T_0} - ik_3 A\omega_1 e^{i\omega_1 T_0} + \text{cc.} \tag{15c}$$

$$(D_0^2+\omega_4^2)v_1 = (-2i\omega_4 D_1 E - i\mu_4\omega_4 C)e^{i\omega_4 T_0} - ik_4 B\omega_2 e^{i\omega_2 T_0} + \text{cc.} \tag{15d}$$

According to Table 1, we thought that the primary resonance case ($\Omega_1 \cong \omega_1$, $\Omega_3 \cong \omega_2$, $\omega_1 \cong \omega_3$ and $\omega_2 \cong \omega_4$) was among the worst resonance situations; cc are the complex conjugates. Using the criteria of resonance

$$\Omega_1 = \omega_1 + \epsilon\sigma_1, \quad \Omega_3 = \omega_2 + \epsilon\sigma_2, \quad \omega_3 = \omega_1 + \epsilon\sigma_3, \quad \omega_4 = \omega_2 + \epsilon\sigma_4 \tag{16}$$

in which σ_1, σ_2, σ_3, and σ_4 are collectively referred to as the detuning parameters, the solvability requirements that arise when secular terms are terminated using Equation (16). When the secular terms in Equation (15) are eliminated, keeping in mind Equation (16), we obtain:

$$-2i\omega_1(D_1 A) - i\mu_1\omega_1 A - 3\lambda_2 A^2\bar{A} + \frac{1}{2}f_1 e^{i\sigma_1 T_1} + iC\omega_3 k_1 e^{i\sigma_3 T_1} = 0 \tag{17a}$$

$$-2i\omega_2(D_1 B) - i\mu_2\omega_2 B + \frac{f_3}{2}e^{i\sigma_3 T_1} + iEk_2\omega_4 e^{i\sigma_4 T_1} = 0 \tag{17b}$$

$$-2i\omega_3(D_1 c) - i\mu_3\omega_3 c - ik_3\omega_1 A e^{-i\sigma_3 T_1} = 0 \tag{17c}$$

$$-2i\omega_4(D_1 E) - i\mu_4\omega_4 E - ik_4\omega_2 B e^{-i\sigma_4 T_1} = 0 \tag{17d}$$

Table 1. Outcome of different types of resonance cases on the system.

Resonance Cases	First Mode of the System (x) Without	Second Mode of the System (y) Without
$\Omega_2 = \omega_1, \Omega_4 = \omega_2$	1.3	0.08
$\Omega_2 = \omega_1, \Omega_3 = \omega_2$	1.3	0.9
$\Omega_2 = 2\omega_1, \Omega_4 = \omega_2$	11	0.2
$\Omega_1 = \omega_1, \Omega_3 = \omega_2$	5.9	1.01
$\Omega_2 = 2\omega_1, \Omega_4 = 2\omega_2$	11	0.5
$\Omega_1 = \omega_1, \Omega_4 = \omega_2$	5.8	0.1

To obtain the modulation equations, we substitute the following polar forms into the secular terms:

$$A = \frac{1}{2}a_1 e^{i\theta_1}, \quad B = \frac{1}{2}a_2 e^{i\theta_2}, \quad C = \frac{1}{2}a_3 e^{i\theta_3}, \quad E = \frac{1}{2}a_4 e^{i\theta_4} \tag{18}$$

$$D_1A(T_1) = \frac{1}{2}[\dot{a}_1 + ia_1\dot{\theta}_1]e^{i\theta_1 T_1}, \quad D_1B(T_1) = \frac{1}{2}[\dot{a}_2 + ia_2\dot{\theta}_2]e^{i\theta_2 T_1} \tag{19}$$

$$D_1C(T_1) = \frac{1}{2}[\dot{a}_3 + ia_3\dot{\theta}_3]e^{i\theta_3 T_1}, \quad D_1E(T_1) = \frac{1}{2}[\dot{a}_4 + ia_4\dot{\theta}_4]e^{i\theta_4 T_1} \tag{20}$$

where a_n and θ_n are functions of the slow time scale T_1, and a_n, θ_n are the steady-state amplitude and phases of motion, respectively (n = 1, 2, 3, 4).

Equating the real and imaginary parts, the following equations are obtained:

$$a_1' = -\frac{\mu_1 a_1}{2} + \frac{f_1}{2\omega_1}\sin\theta_1 + \frac{a_3\omega_3 k_1}{2\omega_1}\cos\theta_3 \tag{21a}$$

$$a_1\theta_1' = \frac{3\lambda_2 a_1^3}{8\omega_1} - \frac{f_1}{2\omega_1}\cos\theta_1 + \frac{a_3\omega_3 k_1}{2\omega_1}\sin\theta_3 \tag{21b}$$

$$a_2' = -\frac{\mu_2 a_2}{2} + \frac{f_3}{2\omega_2}\sin\theta_2 + \frac{k_2\omega_4 a_4}{2\omega_2}\cos\theta_4 \tag{22a}$$

$$a_2\theta_2' = -\frac{f_3}{2\omega_2}\cos\theta_2 + \frac{k_2\omega_4 a_4}{2\omega_2}\sin\theta_4 \tag{22b}$$

$$a_3' = -\frac{\mu_3 a_3}{2} - \frac{k_3\omega_1 a_1}{2\omega_3}\cos\theta_3 \tag{23a}$$

$$a_3\theta_3' = \frac{k_3\omega_1 a_1}{2\omega_3}\sin\theta_3 \tag{23b}$$

$$a_4' = -\frac{\mu_4 a_4}{2} - \frac{k_4\omega_2 a_2}{2\omega_4}\cos\theta_4 \tag{24a}$$

$$a_4\theta_4' = \frac{k_3\omega_1 a_1}{2\omega_3}\sin\theta_4 \tag{24b}$$

where $\phi_1 = \sigma_1 T_1 - \theta_1$, $\phi_2 = \sigma_2 T_1 - \theta_2$, $\phi_3 = \sigma_3 T_1 + \theta_3 - \theta_1$, and $\phi_4 = \sigma_4 T_1 + \theta_4 - \theta_2$.

We may obtain the frequency response equations (FREs) for the practical situation ($a_1 \neq 0, a_2 \neq 0, a_3 \neq 0, a_4 \neq 0$) as follows: when ($\dot{a}_m = 0$ and $\dot{\theta}_m = 0$), the steady-state solution of the system with NDF controllers corresponding to the fixed point of (21)–(24) is obtained.

$$0 = -\frac{\mu_1 a_1}{2} + \frac{f_1}{2\omega_1}\sin\theta_1 + \frac{a_3\omega_3 k_1}{2\omega_1}\cos\theta_3 \tag{25a}$$

$$a_1\sigma_1 = \frac{3\lambda_2 a_1^3}{8\omega_1} - \frac{f_1}{2\omega_1}\cos\theta_1 + \frac{a_3\omega_3 k_1}{2\omega_1}\sin\theta_3 \tag{25b}$$

$$0 = -\frac{\mu_2 a_2}{2} + \frac{f_3}{2\omega_2}\sin\theta_2 + \frac{k_2\omega_4 a_4}{2\omega_2}\cos\theta_4 \tag{26a}$$

$$a_2\sigma_2 = -\frac{f_3}{2\omega_2}\cos\theta_2 + \frac{k_2\omega_4 a_4}{2\omega_2}\sin\theta_4 \tag{26b}$$

$$0 = -\frac{\mu_3 a_3}{2} - \frac{k_3 \omega_1 a_1}{2\omega_3} \cos\theta_3 \tag{27a}$$

$$a_3(\sigma_1 - \sigma_3) = \frac{k_3 \omega_1 a_1}{2\omega_3} \sin\theta_3 \tag{27b}$$

$$0 = -\frac{\mu_4 a_4}{2} - \frac{k_4 \omega_2 a_2}{2\omega_4} \cos\theta_4 \tag{28a}$$

$$a_4(\sigma_2 - \sigma_4) = \frac{k_3 \omega_1 a_1}{2\omega_3} \sin\theta_4 \tag{28b}$$

When we square and add (27a)–(27b) and (28a)–(28b), we obtain

$$a_3^2 = (k_3^2 \omega_1^2 a_1^2)/\{4\omega_3^2[\mu_3^2/4 + (\omega_1 - \omega_3)^2]\} \tag{29}$$

$$a_4^2 = (k_4^2 \omega_2^2 a_2^2)/\{4\omega_4^2[\mu_4^2/4 + (\omega_2 - \omega_4)^2]\} \tag{30}$$

$$\cos\phi_3 = -\frac{\mu_3 \omega_3 a_2}{k_3 \omega_1 a_1} \tag{31a}$$

$$\sin\phi_3 = \frac{2\omega_3(\sigma_1 - \sigma_3)a_3}{k_3 \omega_1 a_1} \tag{31b}$$

$$\cos\phi_4 = -\frac{\mu_4 \omega_4 a_4}{k_4 \omega_2 a_2} \tag{32a}$$

$$\sin\phi_4 = \frac{2\omega_4(\sigma_2 - \sigma_4)a_4}{k_4 \omega_2 a_2} \tag{32b}$$

When (31) and (32) are inserted into (25) and (26), the squared results are added together to yield

$$\left(\frac{\mu_1 a_1}{2} + \frac{\mu_3 \omega_3^2 k_1 a_3^2}{4\omega_3^2 a_1 k_3}\right)^2 + \left(-a_1\sigma_1 + \frac{3\lambda_2 a_1^3}{8\omega_1} + \frac{a_3^2 \omega_3^2 k_1(\sigma_1 - \sigma_3)}{k_3 a_1 \omega_1^2}\right)^2 = \frac{f_1^2}{4\omega_1^2} \tag{33}$$

$$\left(\frac{\mu_2 a_2}{2} + \frac{\mu_4 \omega_4 k_2 a_4}{2k_4 \omega_2^2}\right)^2 + \left(-a_2\sigma_2 + \frac{k_2 \omega_4^2(\sigma_2 - \sigma_4)a_4}{k_4 \omega_2^2 a_2}\right)^2 = \frac{f_3^2}{4\omega_2^2} \tag{34}$$

The following forms are introduced in order to ascertain the steady-state solution's stability:

$$a_m = a_{m0} + a_{m1}, \quad \phi_m = \phi_{m0} + \phi_{m1} \tag{35}$$

where a_{m0} and ϕ_{m0} represent the solutions of Equations (21)–(24) and a_{m0} and ϕ_{m0} represent perturbations that are thought to be minimal in relation to a_{m0} and ϕ_{m0}. By replacing (35) with (21)–(24) and retaining only the linear terms in a_{m0} and ϕ_{m0}, we obtain:

$$\dot{a}_{11} = \left[-\frac{\mu_1}{2}\right] a_{11} + \left[\frac{f_1}{2\omega_1} \cos\phi_1\right] \phi_{11} + \left[\frac{\omega_3 k_1 \cos\phi_3}{2\omega_1}\right] a_{31} - \left[\frac{a_3 \omega_3 k_1 \sin\phi_3}{2\omega_1}\right] \phi_{31} \tag{36}$$

$$\dot{\phi}_{11} = \left[\frac{\sigma_1}{a_1} - \frac{9\lambda_2 a_1}{8\omega_1}\right] a_{11} - \left[\frac{f_1}{2\omega_1 a_1} \sin\phi_1\right] \phi_{11} - \left[\frac{\omega_3 k_1 \sin\phi_3}{2\omega_1 a_1}\right] a_{31} - \left[\frac{a_3 \omega_3 k_1 \cos\phi_3}{2\omega_1 a_1}\right] \phi_{31} \tag{37}$$

$$\dot{a}_{21} = \left[-\frac{\mu_2}{2}\right] a_{21} + \left[\frac{f_3}{2\omega_2} \cos\phi_2\right] \phi_{21} + \left[\frac{k_2 \omega_4 \cos\phi_4}{2\omega_2}\right] a_{41} + \left[\frac{k_2 \omega_4 a_4 \sin\phi_4}{2\omega_2}\right] \phi_{41} \tag{38}$$

$$\dot{\phi}_{21} = \left[\frac{\sigma_2}{a_2}\right] a_{21} - \left[\frac{f_3}{2\omega_2 a_2}\sin\phi_2\right]\phi_{21} - \left[\frac{k_2\omega_4\sin\phi_4}{2\omega_2 a_2}\right] a_{41} - \left[\frac{k_2\omega_4 a_4\cos\phi_4}{2\omega_2 a_2}\right]\phi_{41} \tag{39}$$

$$\dot{a}_{31} = \left[\frac{-k_3\omega_1\cos\phi_3}{2\omega_3}\right] a_{11} - \left[\frac{\mu_3}{2}\right] a_{31} + \left[\frac{k_3 a_1\omega_1\sin\phi_3}{2\omega_3}\right]\phi_{31} \tag{40}$$

$$\begin{aligned}\dot{\phi}_{31} = &\left[-\frac{6\lambda_2 a_1}{8\omega_1} - \frac{f_1}{2\omega_1 a_1^2}\cos\phi_1 + \frac{\omega_3 k_1 a_3}{2\omega_1 a_1^2}\sin\phi_3 + \frac{\omega_1 k_3\sin\phi_3}{2\omega_3 a_3}\right] a_{11} \\ &- \left[\frac{f_1\sin\phi_1}{2\omega_1 a_1}\right]\phi_{11} + \left[\frac{\sigma_3}{a_3} - \frac{3\lambda_2 a_1^2}{8\omega_1 a_3} + \frac{f_1}{2\omega_1 a_1}\cos\phi_1 - \frac{2\omega_3 k_1\sin\phi_3}{2\omega_1 a_1}\right] a_{31} \\ &+ \left[\frac{k_3 a_1\omega_1\cos\phi_3}{2\omega_3 a_3} - \frac{\omega_3 k_1 a_3\cos\phi_3}{2\omega_1 a_1}\right]\phi_{31}\end{aligned} \tag{41}$$

$$\dot{a}_{41} = \left[\frac{-k_4\omega_2\cos\phi_4}{2\omega_4}\right] a_{21} + \left[\frac{-\mu_4}{2}\right] a_{41} + \left[\frac{k_4\omega_2 a_2\sin\phi_4}{2\omega_4}\right]\phi_{41} \tag{42}$$

$$\begin{aligned}\dot{\phi}_{41} = &\left[\frac{k_2\omega_4 a_4\sin\phi_4}{2\omega_2 a_2^2} - \frac{f_3}{2\omega_2 a_2^2}\cos\phi_2 + \frac{k_4\omega_2\sin\phi_4}{2\omega_4 a_4}\right] a_{21} \\ &- \left[\frac{f_3}{2\omega_2 a_2}\sin\phi_2\right]\phi_{21} + \left[\frac{\sigma_4}{a_4} + \frac{f_3}{2\omega_2 a_2 a_4}\cos\phi_2 - \frac{k_2\omega_4\sin\phi_4}{2\omega_2 a_2}\right] a_{41} \\ &+ \left[\frac{k_4\omega_2 a_2\cos\phi_4}{2\omega_4 a_4} - \frac{k_2\omega_4 a_4\cos\phi_4}{2\omega_2 a_2}\right]\phi_{41}\end{aligned} \tag{43}$$

The matrix can represent the previous system:

$$\begin{bmatrix}\dot{a}_{11}\\ \dot{\phi}_{11}\\ \dot{a}_{21}\\ \dot{\phi}_{21}\\ \dot{a}_{31}\\ \dot{\phi}_{31}\\ \dot{a}_{41}\\ \dot{\phi}_{41}\end{bmatrix} = [J]\begin{bmatrix}a_{11}\\ \phi_{11}\\ a_{21}\\ \phi_{21}\\ a_{31}\\ \phi_{31}\\ a_{41}\\ \phi_{41}\end{bmatrix} \tag{44}$$

where [J] stands for the Jacobian matrix associated with Equations (34)–(42). The eigenvalues of [J] can be written as follows:

$$\lambda^8 + R_1\lambda^7 + R_2\lambda^6 + R_3\lambda^5 + R_4\lambda^4 + R_5\lambda^3 + R_6\lambda^2 + R_7\lambda + R_8 = 0 \tag{45}$$

where $R_1, R_2, R_3, R_4, R_5, R_6, R_7$, and R_8 are coefficients of (45). All eigenvalues must have negative real portions in order for the solution to be stable; otherwise, instability results. This condition is satisfied if and only if the determinant (D) and all of its primary minors are rigorously positive, according to the Routh–Hurwitz criterion, guaranteeing that all roots of Equation (45) are located in the left side of the complex plane.

$$D = \begin{vmatrix} R_1 & 1 & 0 & 0 & 0 & 0 & 0 & 0 \\ R_3 & R_2 & R_1 & 1 & 0 & 0 & 0 & 0 \\ R_5 & R_4 & R_3 & R_2 & R_1 & 1 & 0 & 0 \\ R_7 & R_6 & R_5 & R_4 & R_3 & R_2 & R_1 & 1 \\ 0 & R_8 & R_7 & R_6 & R_5 & R_4 & R_3 & R_2 \\ 0 & 0 & 0 & R_8 & R_7 & R_6 & R_5 & R_4 \\ 0 & 0 & 0 & 0 & 0 & R_8 & R_7 & R_6 \\ 0 & 0 & 0 & 0 & 0 & 0 & 0 & R_8 \end{vmatrix} \tag{46}$$

In this case, the characteristic coefficients R_i $(i = 1, 2, \ldots, 8)$ from Equation (45) directly make up the elements of the Routh–Hurwitz matrix D. Owing to the system's high dimensionality, MATLAB is used to numerically estimate these coefficients and the major minors of the determinant D at each parameter point. After that, the parameter space is scanned to create the stability maps. Regions with strictly positive determinants and minors are mapped as stable, and any violation indicates the unstable borders.

3. Results and Discussion

The steady-state amplitudes (a_1,a_2) against detuning parameters (σ_1,σ_2) and the temporal response for both an electromechanical system and controller are graphically displayed in this section. The ODE45 MATLAB [39] solver was used to numerically solve the system's initial Equations (1) and (2). Here, the FR function solutions pertaining to the stability of the electromechanical system and the controller are analyzed, as well as the numerical solution of the mathematical modeling and its stability. In addition to reporting and discussing several resonance examples, the impacts of different parameters on the steady-state solution are obtained and examined, and a comparison between different controllers is made.

3.1. System Behavior with and Without NDF Control

The "fourth-order Runge–Kutta (RK-4)" method is used to find numerical solutions for the primary resonance case of the main system, combined with NDF controllers ($\Omega_1 \cong \omega_1$, $\Omega_3 \cong \omega_2, \omega_1 \cong \omega_3$ and $\omega_2 \cong \omega_4$). The ode45 solver in MATLAB (R2025b) is used to do this study using the particular system parameters mentioned below:

$$(\mu_1 = 0.031; \mu_2 = 0.4; f_1 = 3.5; \omega_1 = 5.05; \lambda_1 = 0.00315; \lambda_2 = 0.025; \omega_2 = 3.75; \mu_2 = 0.4; \omega_2 = 4.05;$$
$$\beta_0 = 0.0072; \beta_1 = 0.005; \beta_2 = 0.0015; f_3 = 1.6; f_4 = 3.1; \omega_3 = 4.05; \omega_4 = 2.45; \epsilon = 0.5;$$
$$k_1 = 5; k_2 = 5; k_3 = 2; k_4 = 2; \omega_3 = 5.05; \omega_4 = 4.05; \mu_3 = 0.01; \mu_4 = 0.02)$$

Figure 3 shows the resulting phase plane and response for the non-resonant case.

Figure 4 shows the system's steady-state amplitudes at the worst resonance condition (about 5.9 and 1, respectively) prior to the implementation of NDF controllers. The system amplitudes are then greatly reduced to 0.01 and 0.02, respectively, with the inclusion of NDF controllers. With $E_a = 590$, $E_a = 51.5$, and a decrease in vibrations of almost 99.8% and 98%, respectively, relative to their uncontrolled value, this demonstrates the efficacy of the NDF controllers.

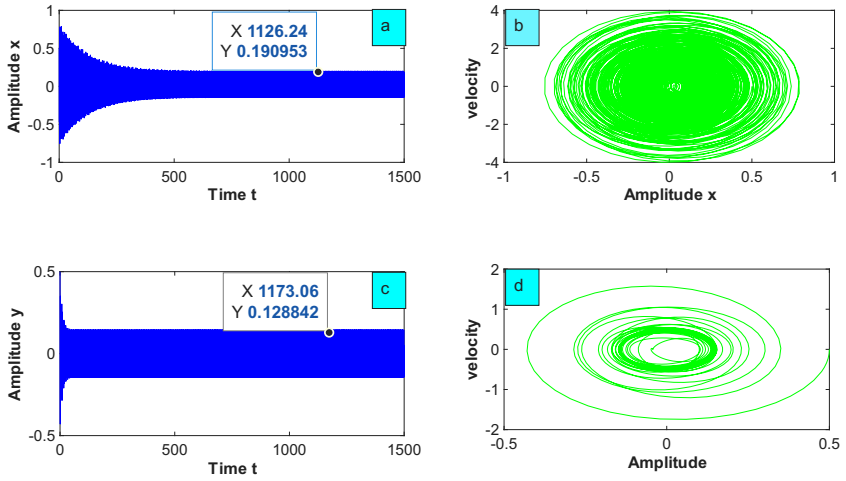

Figure 3. The uncontrolled system's reaction and phase without any resonance for the first and second modes, respectively: (**a**) Time history of amplitude x; (**b**) Phase plane of amplitude x; (**c**) Time history of amplitude y; (**d**) Phase plane of amplitude y.

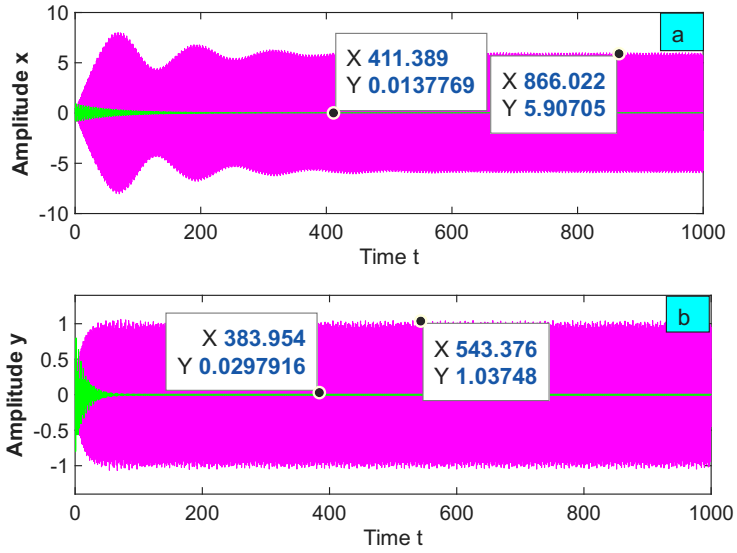

Figure 4. The amplitude of the focal system at PR worst resonance: (**a**) the amplitude of the first mode before and after NDF; (**b**) the amplitude of the second mode before and after NDF.

3.2. Frequency Response Curves

The excitation force (f) and the detuning parameters σ_1, σ_2 are the main factors influencing the response amplitudes of the system and the NDF controller. We may monitor the evolution of these amplitudes by numerically calculating the frequency response equations (FREs) and graphing the results. The presence of two peaks in the plots is a clear indication of the coupling effect between the system and the NDF controller. The frequency response of the system before and after control is shown in Figure 5. The system showed extreme instability at resonance in the uncontrolled condition, with the amplitude reaching roughly 6 for the first mode and 1 for the second mode. Both responses had a notable decrease to almost zero at ($\sigma_1 = \sigma_2 = 0$) after the NDF controller was applied, along with a peak-splitting phenomena. The initial unstable peak split into two stable lateral peaks for the $(a_1 - \sigma_1)$, with an unstable center region between them. The $(a_2 - \sigma_2)$ response, on the other hand, changed to a non-symmetrical stability pattern; the system recovered stability in the positive frequency branch, while the negative frequency branch continued to be unstable. These findings demonstrate how well the controller suppresses resonance and modifies the stability map to create previously nonexistent safe operating windows. The FR behavior of the primary system combined with an NDF controller is shown in Figure 6, where solid lines (burgundy) represent stable solutions and any other color in the first mode indicates instability. The response curves for the primary system are shown in Figure 6a, while the frequency response of the controller is the subject of Figure 6b.

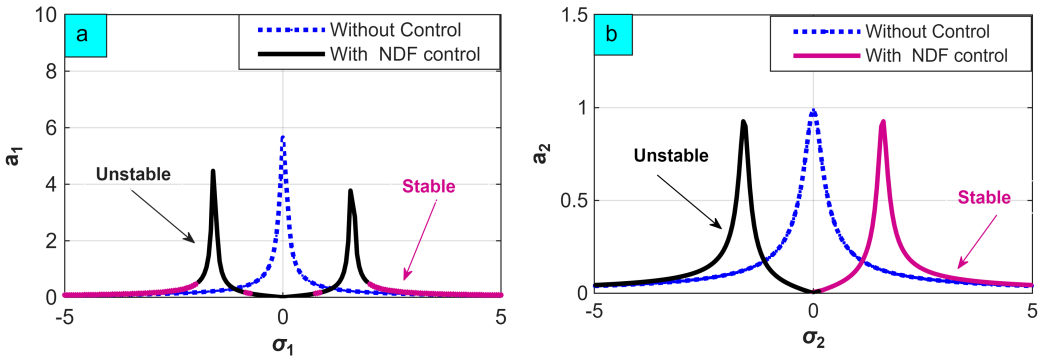

Figure 5. FRC of the system without and with NDF controller: (**a**) frequency response curve for amplitude $(a_1 - \sigma_1)$; (**b**) frequency response curve for amplitude $(a_2 - \sigma_2)$.

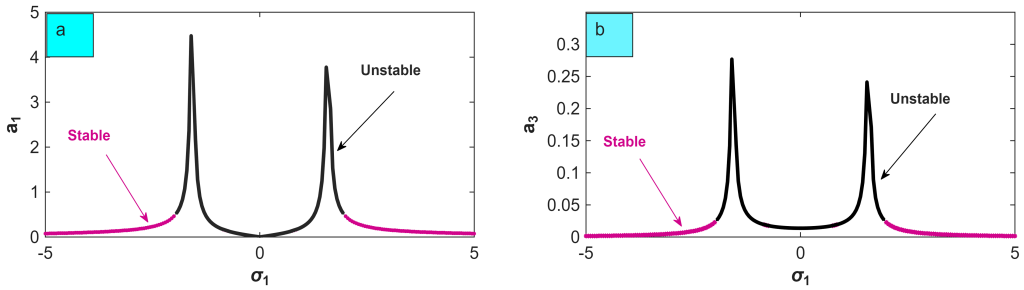

Figure 6. FRC for (**a**) the first mode system $(a_1 - \sigma_1)$ and (**b**) the NDF controller $(a_3 - \sigma_1)$ ($f_1 = 3.5$, $\omega_1 = 5.05$, $\mu_1 = 0.0031$, $k_1 = 5$, $k_3 = 2$).

Figures 7 and 8 show that the vibration frequency decreases as the damping coefficient increases. With a focus on the stable regions, these graphs provide a visual evaluation of the system's performance over a range of frequencies. The findings show that when $\sigma_1 = 0$, the primary system obtains its minimal vibration amplitude. This demonstrates how well the NDF controller reduces oscillations during PR resonance. The amplitudes of the primary system and the NDF controller rise proportionately to an increase in the harmonic excitation force, as shown in Figure 9a,b. Interestingly, near the resonance point ($\sigma_1 = 0$), the fundamental system reaches its lowest vibration amplitude. Figure 10a,b shows the impact of the control signal gain, K_1. These findings show how the parameters of the NDF controller determine the dynamic behavior of the system. In particular, Figure 10a displays a shift in the controller's amplitude to the right, signifying an increase in the bandwidth of the control signal. Additionally, Figure 10b verifies that the NDF controller's amplitude diminishes monotonically, which is in line with the main goal of the control gain. Figure 11a shows that increasing the feedback signal K_3 causes the vibration reduction frequency to shift toward higher values. Higher feedback rates therefore cause the controller's reaction amplitudes to increase, as illustrated in Figure 11b. The initial coupled pair (k_1, k_3) is resilient and has strong parametric sensitivity, which is explicitly confirmed by this widening of the resonance bandwidth. Additionally, limiting these gain values avoids actuator saturation by guaranteeing that the generated control force stays within a reasonable range. The impact of the nonlinear coefficient on the dynamic response of the system is seen in Figure 12. It is found that the vibration amplitudes consistently decrease as this coefficient is increased. In particular, the peak amplitudes for both the main system and the NDF controller considerably reduce as these values rise, indicating the controller's greater capacity to suppress oscillations. Additionally, Figure 13 examines how the system is affected by the natural frequency ω_1. The findings show that while the NDF controller is largely unaffected by these modifications, raising ω_1 causes the main system's vibration amplitude to decrease.

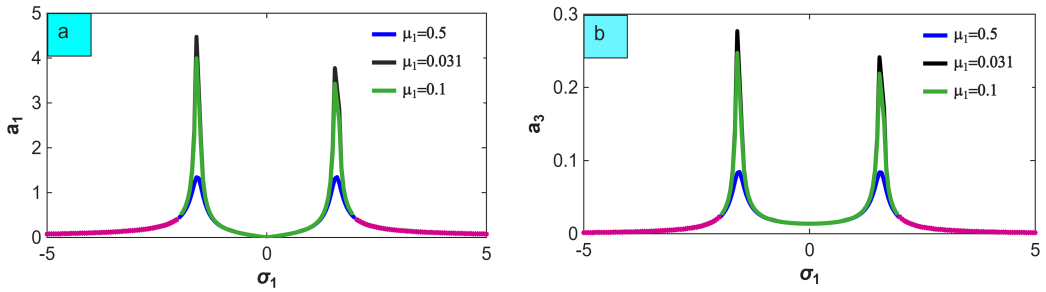

Figure 7. The act of changing the values of the damping coefficient μ_1: (**a**) the first mode system with NDF controller $(a_1 - \sigma_1)$ and (**b**) the controller $(a_3 - \sigma_1)$.

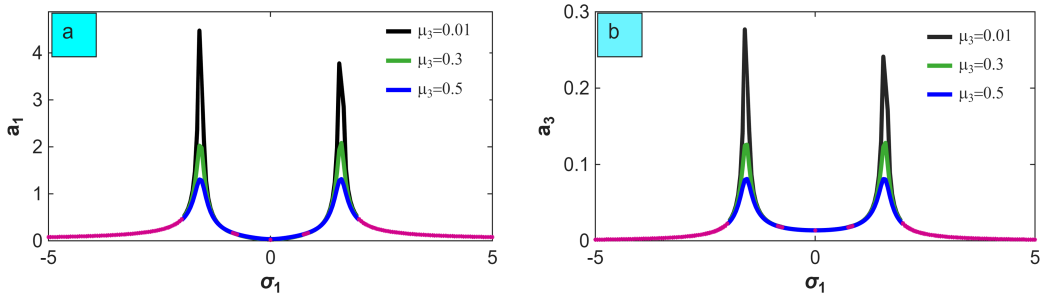

Figure 8. A change in the values of the damping coefficient μ_3: (**a**) the first mode system with NDF controller $(a_1 - \sigma_1)$ and (**b**) the controller $(a_3 - \sigma_1)$.

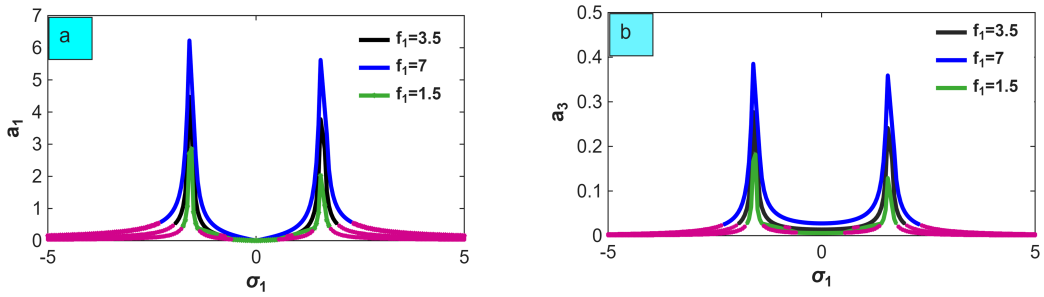

Figure 9. A changing in the values of external force f_1: (**a**) the first mode system with NDF controller $(a_1 - \sigma_1)$ and (**b**) the controller $(a_3 - \sigma_1)$.

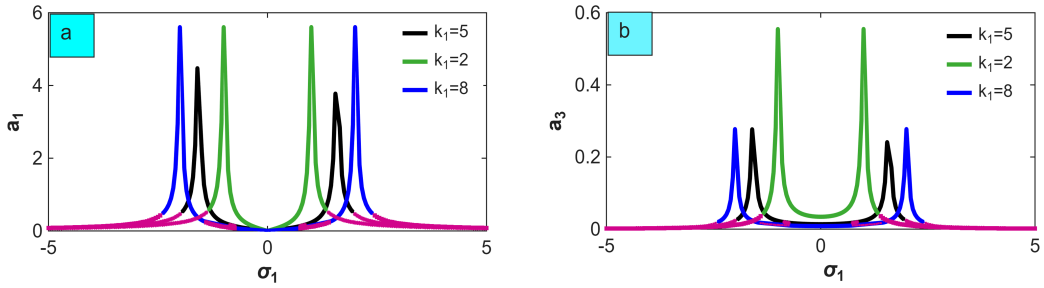

Figure 10. A change in the values of gain k_1: (**a**) the first mode system with NDF controller $(a_1 - \sigma_1)$ and (**b**) the controller $(a_3 - \sigma_1)$.

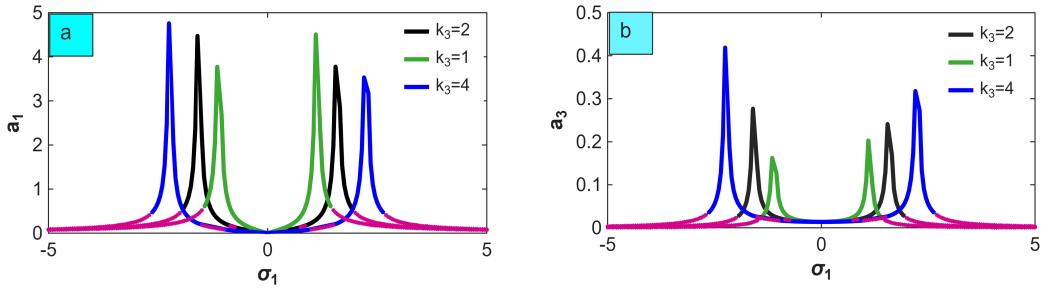

Figure 11. A change in the values of gain k_3: (**a**) the first mode system with NDF controller $(a_1 - \sigma_1)$ and (**b**) the controller $(a_3 - \sigma_1)$.

Figure 14 shows the FR of the system on the second mode Figure 14a and NDF controller Figure 14b as functions of the detuning parameter σ_2. The response begins with an unstable phase on the left, whereas the burgundy line on the right indicates the stable region, where the amplitude shows a dramatic peak close to the resonance point and great sensitivity. The solid line on the right represents the system's transition toward a stable state as σ_2 rises, signifying the restoration of equilibrium. Figures 15–19 indicate the effect of changing the parameter on the frequency response of system in the first mode and controller. As shown in Figure 15a,b, when the values of the force increase, the amplitude of the system

and controller are increased. Figures 16 and 18 show that the steady-state amplitudes for the controller and the main system on the second mode increase as the damping coefficients μ_3 and μ_4 increase. The FR of the amplitudes a_2 and a_4 as functions of the detuning parameter σ_2 for different values of the coefficient k_2 is shown in Figure 18a,b. The resonance peaks are found to shift significantly laterally away from the center ($\sigma_2 = 0$) toward higher frequency values when k_2 is increased from 2 to 8. The controller's amplitude a_4 exhibits a noticeable drop in its highest values as k_2 increases, whereas the peak magnitudes of a_2 stay mostly constant throughout these variations. This result suggests that k_2 improves the system's operational stability over a wider frequency range by efficiently adjusting the resonance positions and lowering the oscillation burden on the controller. As the NDF gain increases, Figure 19a demonstrates that the vibration reduction frequency bandwidth of the NDF control for the main system's amplitude widens. The controller peak amplitudes rise with high NDF gain settings, as seen in Figure 19b. The initial coupled pair (k_2, k_4) is resilient and has strong parametric sensitivity, which is explicitly confirmed by this widening of the resonance bandwidth. Additionally, limiting these gain values avoids actuator saturation by guaranteeing that the generated control force stays within a reasonable range.

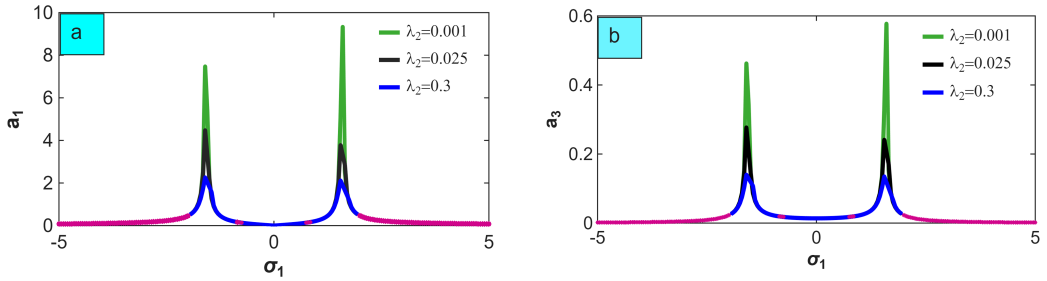

Figure 12. The act of changing the values of the nonlinear coefficient λ_2: (**a**) the first mode system with NDF controller $(a_1 - \sigma_1)$ and (**b**) the controller $(a_3 - \sigma_1)$.

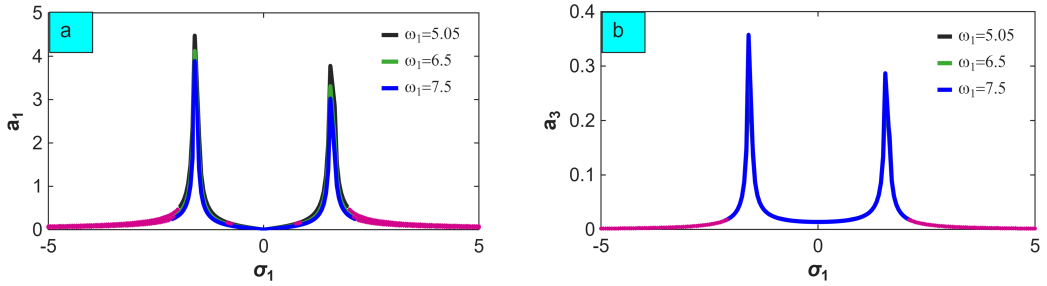

Figure 13. The act of changing the values of natural frequencies ω_1: (**a**) the first mode system with NDF controller $(a_1 - \sigma_1)$ and (**b**) the controller $(a_3 - \sigma_1)$.

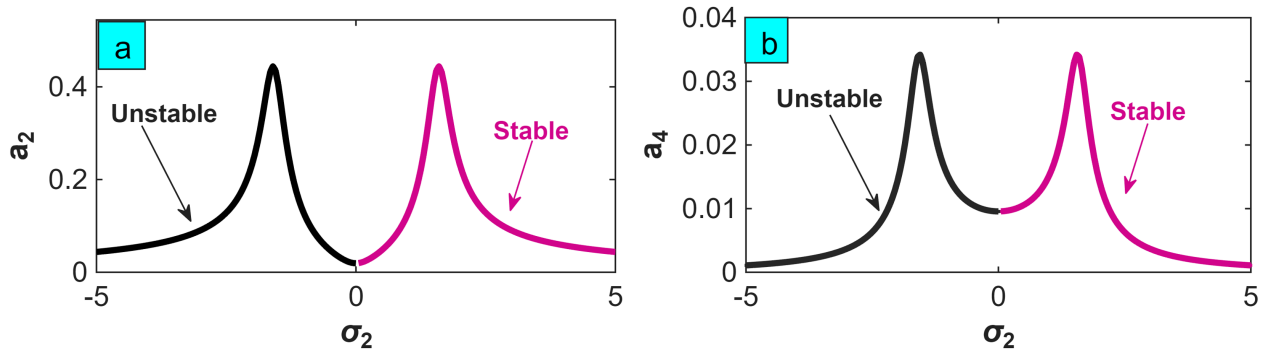

Figure 14. FRC for (**a**) the second mode system$(a_2 - \sigma_2)$ and (**b**) the NDF controller $(a_4 - \sigma_2)$ at $(f_3 = 1.6, \omega_3 = 4.05, \mu_2 = 0.4, k_2 = 5, k_4 = 2)$.

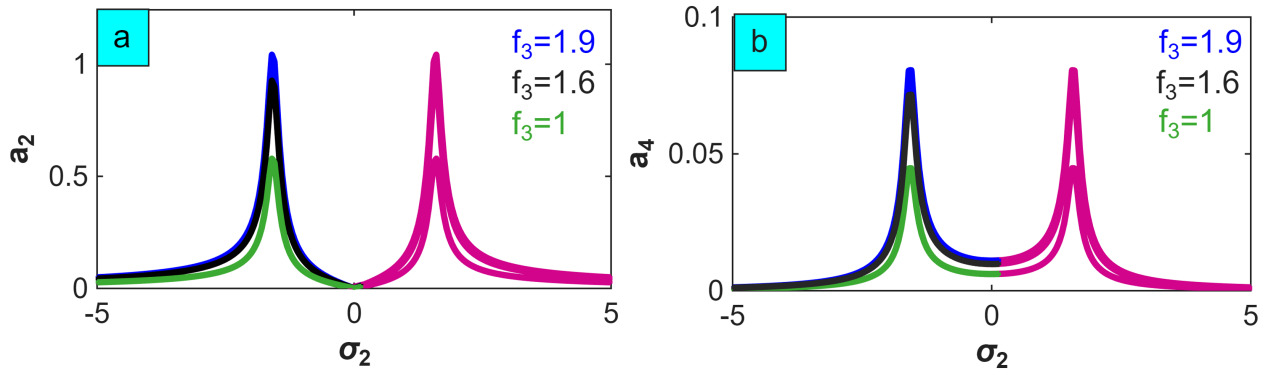

Figure 15. The act of varying the values of external force f_3: (**a**) the second mode system with NDF controller $(a_2 - \sigma_2)$ and (**b**) the controller $(a_2 - \sigma_4)$.

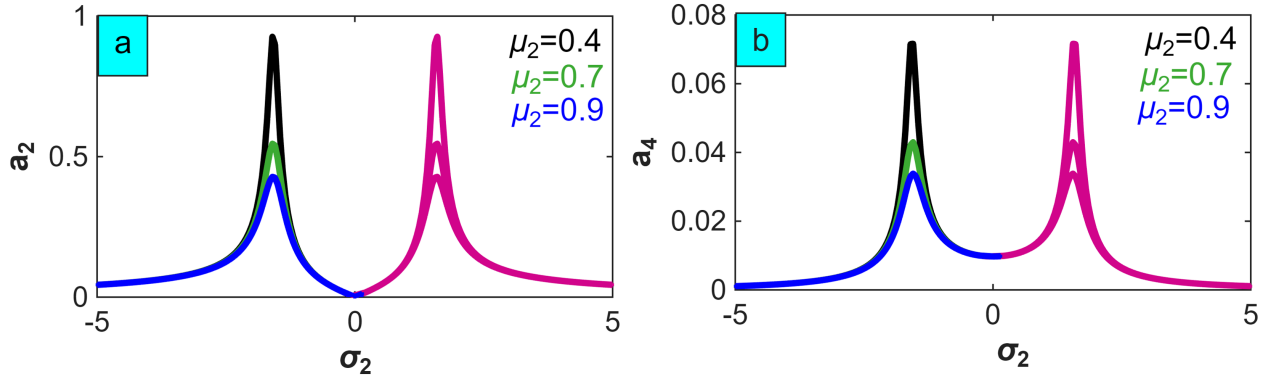

Figure 16. The act of varying the values of the damping coefficient μ_2: (**a**) the second mode system with NDF controller $(a_2 - \sigma_2)$ and (**b**) the controller $(a_2 - \sigma_4)$.

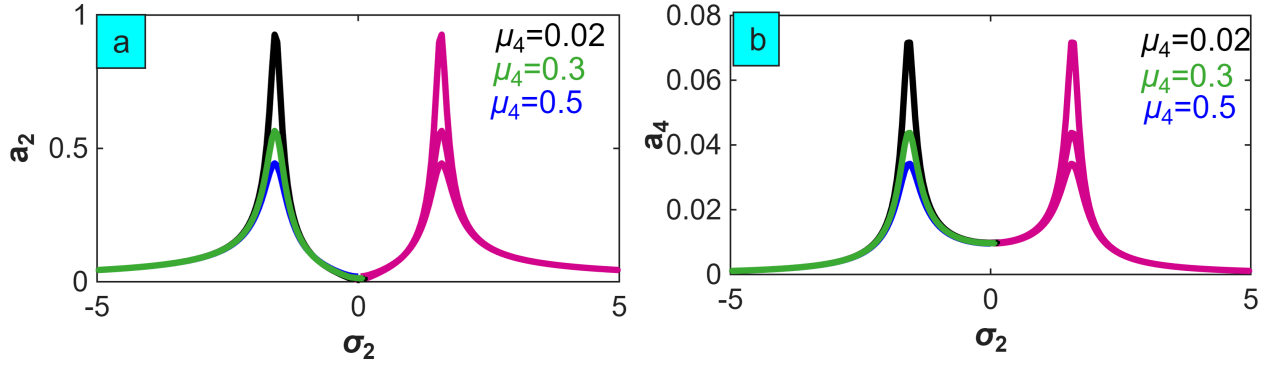

Figure 17. The act of varying the values of the damping coefficient μ_4: (**a**) the second mode system with NDF controller $(a_2 - \sigma_2)$ and (**b**) the controller $(a_2 - \sigma_4)$.

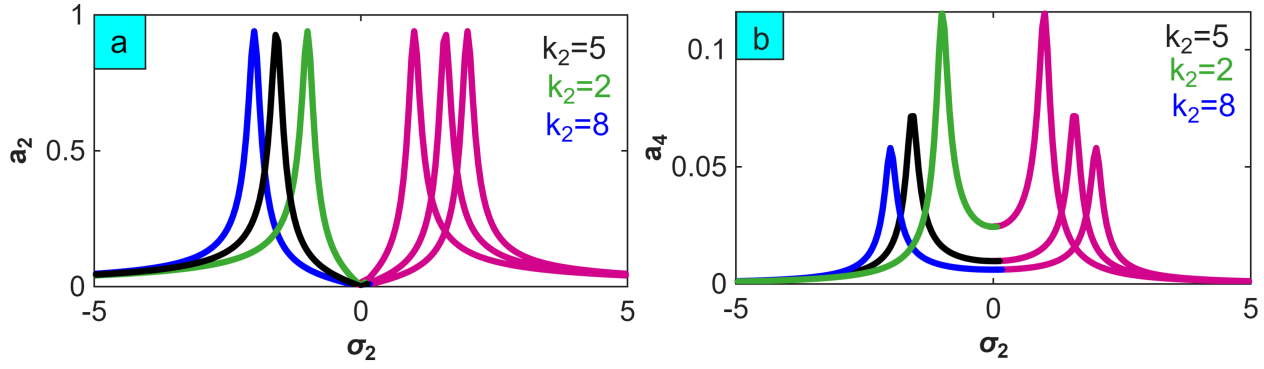

Figure 18. The act of varying the values of gain k_2: (**a**) the second mode system with NDF controller $(a_2 - \sigma_2)$ and (**b**) the controller $(a_2 - \sigma_4)$.

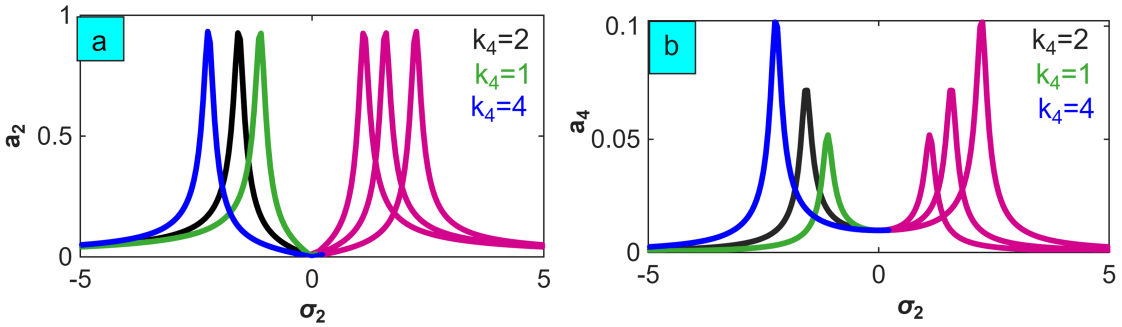

Figure 19. The act of varying the values of gain k_4: (**a**) the second mode system with NDF controller $(a_2 - \sigma_2)$ and (**b**) the controller $(a_2 - \sigma_4)$.

4. Effects of Different Parameter

The impacts of various parameters on the system response are displayed in this section. Figure 20 demonstrates that the amplitude of the system in steady-state is a monotonically increasing function to the external forces f_1, f_3, respectively. The influence of the parameter μ_1 on the vibration amplitude $x(t)$ is shown in Figure 20c. The amplitude is found to rise slightly at first, peaking at very low values of μ_1, and then drop monotonically as μ_1 rises. This suggests that raising μ_1 improves the stability of the system and successfully reduces vibrations. Figure 20d shows a plot of the response amplitude $y(t)$ against the parameter μ_2. As μ_2 grows, the amplitude of the curve exhibits a nonlinear decline. In the range $[0.5, 1.5]$, the rate of decline is faster, and as μ_2 increases, it becomes more gradual. The effect of the frequency (or parameter) w_1 on $x(t)$ is shown in Figure 20e. As w_1 increases from 5 to 6, a notable linear decrease in the amplitude is seen. The vibration amplitude disappears ($x(t) \approx 0$) beyond $w_1 = 6$, signifying a full vibration suppression zone. As seen in Figure 20, it is preferable to use suitable materials that are cost efficient and to incorporate a particular controller capable of reducing the amplitude when resonance occurs.

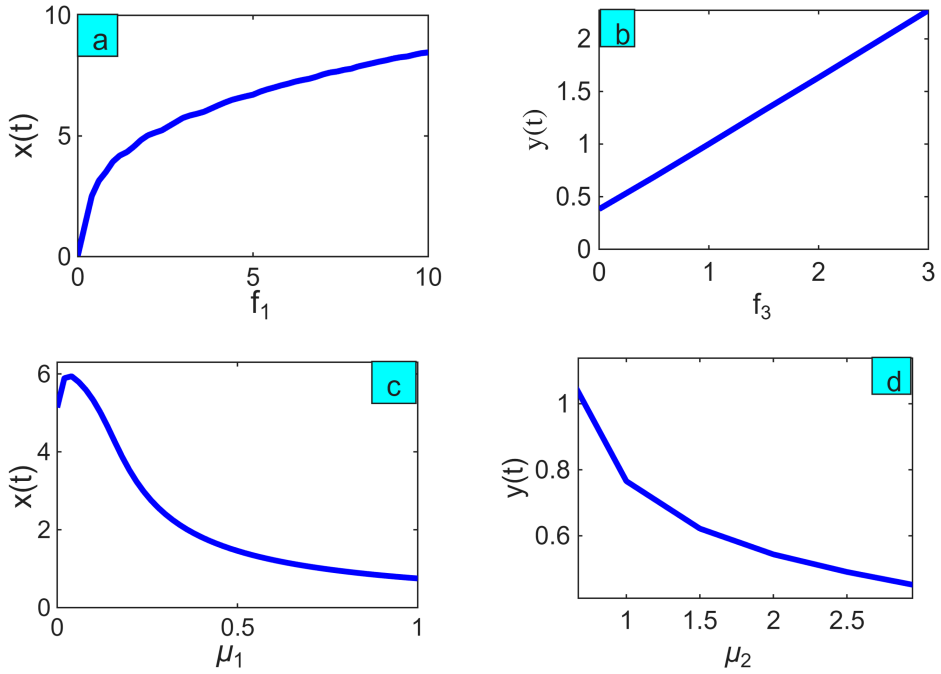

Figure 20. *Cont.*

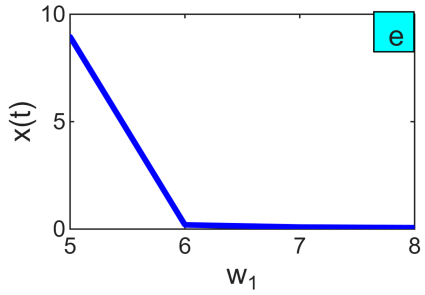

Figure 20. The effects of the parameters of the main system on the amplitude without control: (**a**) external force for the first equation, (**b**) external force for the second equation, (**c**,**d**) for damping coefficient, (**e**) natural frequency.

5. Comparison

5.1. Comparison of Time History Performance for Various Controllers

The system's response with and without control is shown in Figure 21 using low-gain settings. The system first displays uncontrollable nonlinear oscillations across the time span $t \in [0, 300]$. Linear Negative Position Feedback (LNPF) is implemented at $t = 300$ and stays in effect until $t = 600$. The PPF controller then takes over at $t = 1000$ when the LNPF controller is deactivated at $t = 600$. Afterwards, the PPF controller is replaced with the NDF controller. The PPF controller causes a decrease in vibration amplitude during the interval $t \in [600, 1000]$, as seen in the image. Nevertheless, the system's vibrations are more effectively suppressed when the NDF controller is switched on at $t = 1000$.

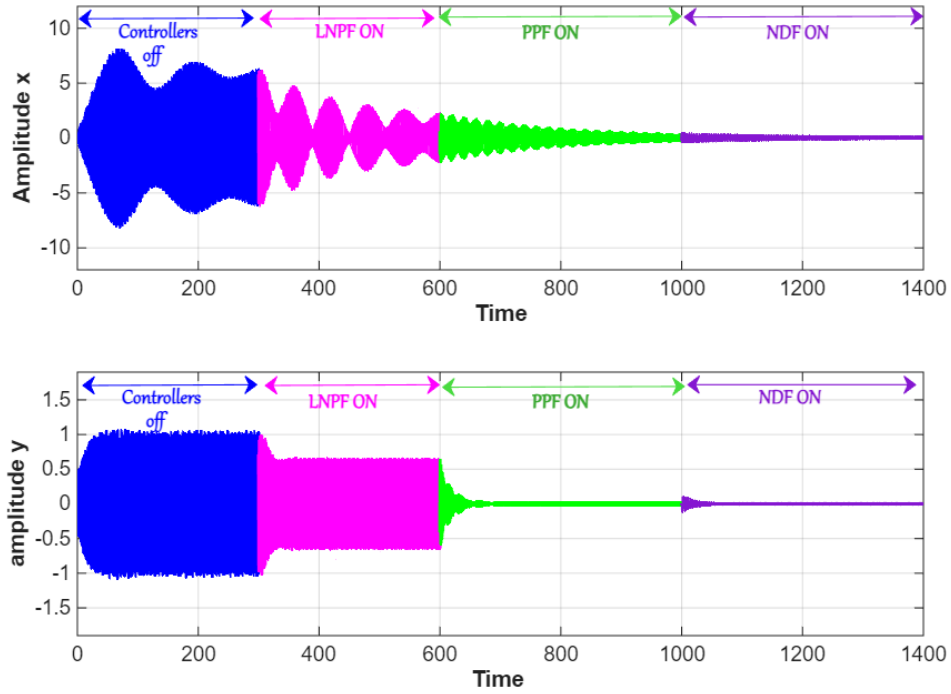

Figure 21. The effects between different types of controllers on the nonlinear electromechanical oscillator for the first and second modes.

5.2. Comparison of (FRCs + Time History) Before and After Control

The FRCs for the electromechanical system before and after regulation against σ_1 and σ_2, respectively, are compared using the numerical simulation of equations in Figures 22 and 23. It shows that the analytical and numerical answers accord quite well, highlighting the strong consistency and agreement between approximate solutions (dashed line) and

numerical simulations (solid line) for both the uncontrolled system and the system with the NDF controller.

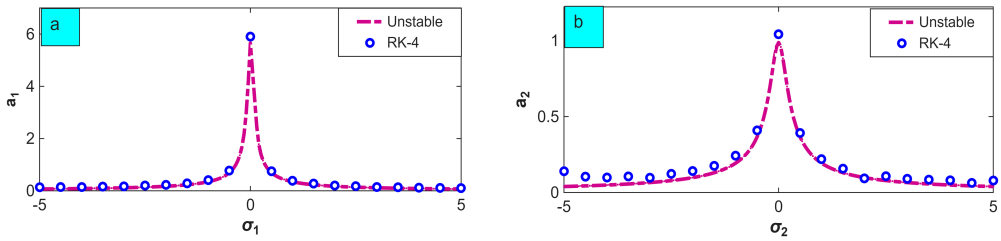

Figure 22. Comparison between the approximate solution (MMS) and the numerical solution (RK-4) before control: (**a**) system amplitude for the first mode $(a_1 - \sigma_1)$ and (**b**) the second mode $(a_2 - \sigma_2)$.

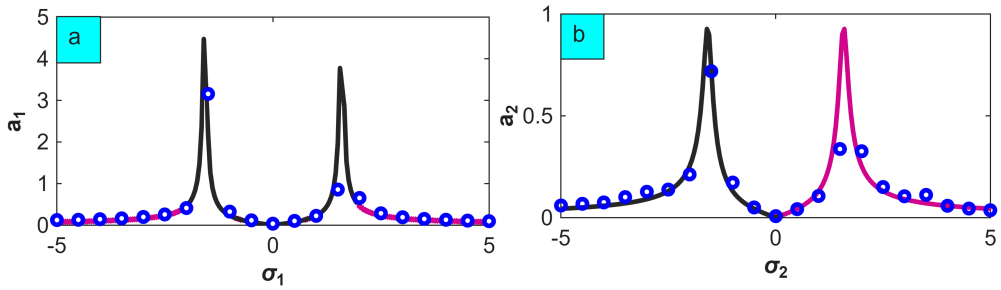

Figure 23. Comparison between the approximate solution (MMS) and the numerical solution (RK-4) after control: (**a**) system amplitude for the first mode $(a_1 - \sigma_1)$ and (**b**) the second mode $(a_2 - \sigma_2)$.

Figures 24 and 25 present a comparison between the numerical and approximate analytical solutions of the uncontrolled system. In addition, Figures 26 and 27 provide the same type of comparison when the NDF controller is incorporated into the system. Overall, Figures 24–27 clearly illustrate the agreement between the numerical and approximate analytical responses over time. In all cases, the system exhibits an initial transient oscillatory response, which gradually decays and eventually settles into steady-state behavior.

The numerical results shown in Figures 24a, 25a, 26a, and 27a capture the complete nonlinear dynamics of the system, including the large initial oscillations that diminish due to damping effects. On the other hand, the approximate solutions in Figures 24b, 25b, 26b, and 27b closely track the same response trends, demonstrating that the analytical approximation effectively represents the dominant system behavior.

The absolute error plots in Figures 24c, 25c, 26c, and 27c further validate this agreement quantitatively. The error is relatively large during the early transient stage, where the oscillations are strongest, then gradually decreases as time progresses, eventually approaching values close to zero. This confirms the high long-term accuracy of the approximation. Moreover, the zoomed time history comparisons in Figures 24d, 25d, 26d, and 27d reveal an excellent match between both solutions in the steady-state region, where the two curves become nearly indistinguishable. In addition to the graphical comparisons, quantitative validation is carried out to evaluate the tracking efficiency of the suggested NDF controller incorporated into the first equation (x-mode). The time history charts of Figures 26 and 27 amply demonstrate how well the analytical MTSM solution aligns with the numerical RK-4 simulation in the controlled state. The discrete values of both solutions and the corresponding absolute error are extracted at certain time intervals and compiled in Tables 2 and 3 in order to assess this agreement with high numerical rigor. The mathematical precision and consistency of the perturbation analysis for the controlled system are rigorously confirmed by the tabulated results, which show that the absolute error is astonishingly minimal. In summary, the results confirm that the approximate analytical model provides a dependable

representation of the full numerical solution, particularly after the transient dynamics have decayed.

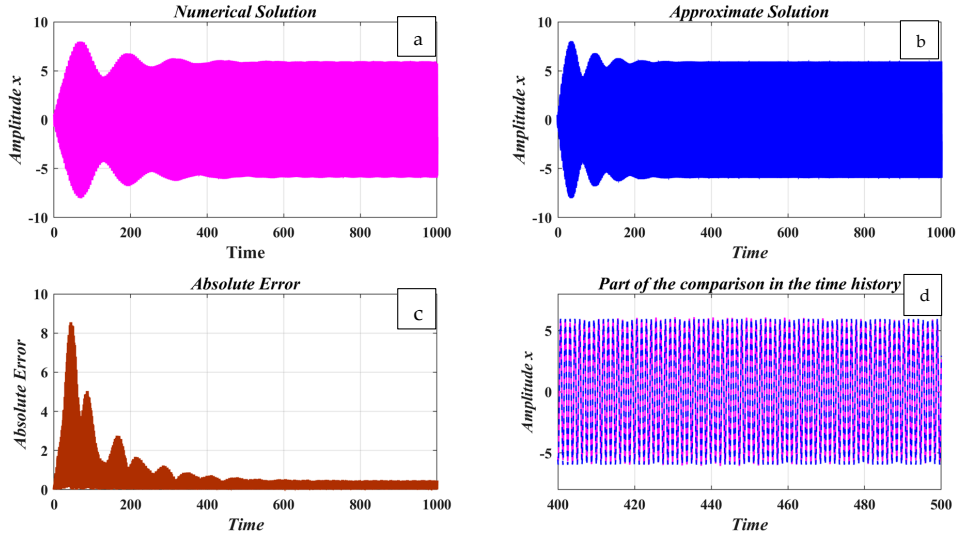

Figure 24. Dynamic response of the first governing equation prior to control activation, comprising (**a**) numerical simulation, (**b**) approximate analytical solution, (**c**) absolute evaluation error, and (**d**) a magnified view of the time history comparison.

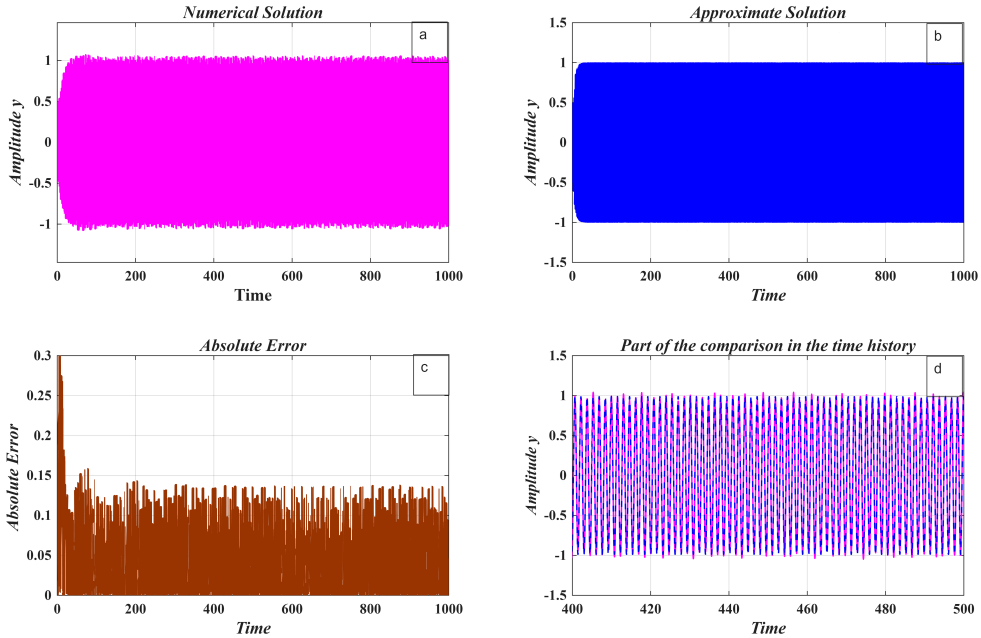

Figure 25. Dynamic response of the second governing equation prior to control activation, comprising (**a**) numerical simulation, (**b**) approximate analytical solution, (**c**) absolute evaluation error, and (**d**) a magnified view of the time history comparison.

Table 2. Quantitative verification and comparison of absolute errors between RK-4 and MTSM solutions for the controlled system (after the first mode implementation of the NDF controller).

Time	RK-4	MSM	Absolute Error
192	0.068160	0.068174	0.000014
233	0.046146	0.046171	0.000026
305	0.012004	0.012011	0.000007
398	0.011008	0.011047	0.000039
441	0.009833	0.006863	0.002970

Table 2. *Cont.*

Time	RK-4	MSM	Absolute Error
514	0.010207	0.002507	0.007700
601	0.010609	0.001008	0.009600
644	0.010716	0.000481	0.010236
765	0.010259	−0.000364	0.010623
808	0.010275	−0.000384	0.010660
901	0.010639	−0.000063	0.010702
973	0.010108	−0.000503	0.010611

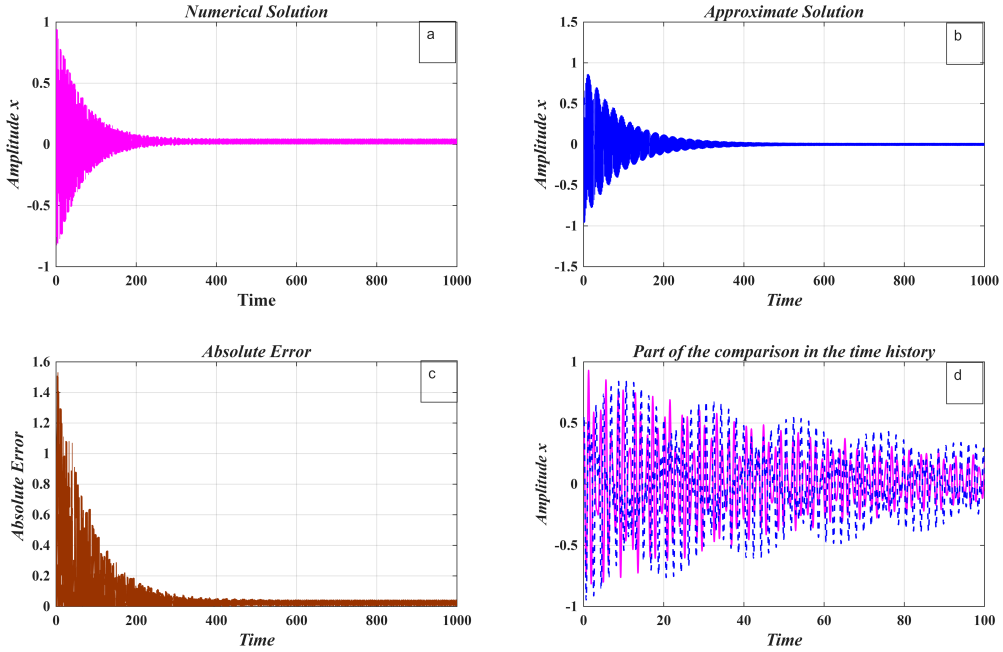

Figure 26. Verification of the controlled response for the first equation. A comparative analysis between (**a**) numerical and (**b**) approximate methods, alongside (**c**) the absolute error profile and (**d**) transient time history details.

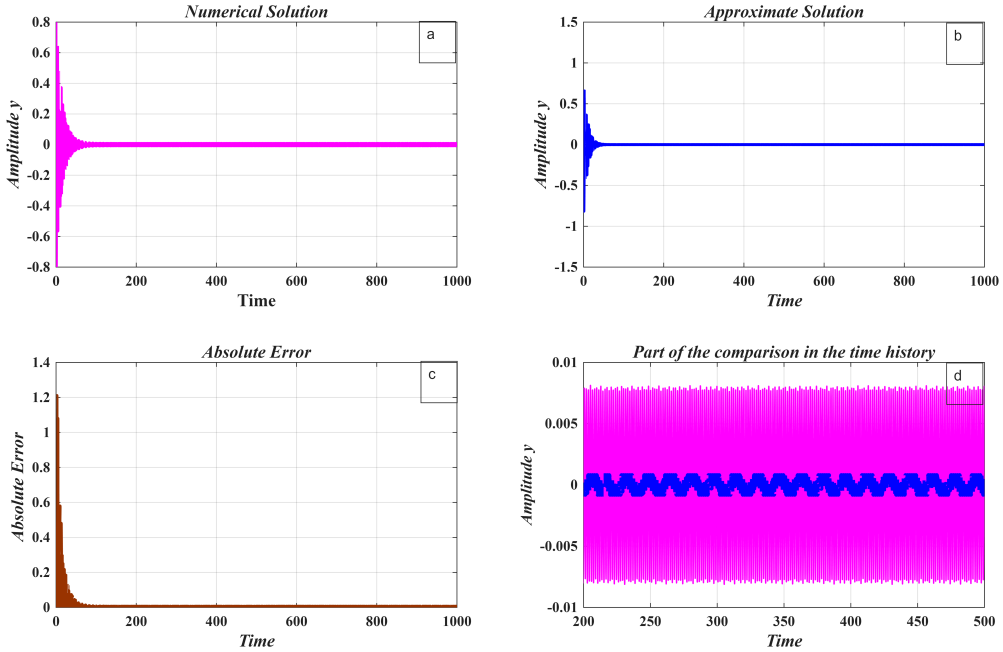

Figure 27. Verification of the controlled response for the second equation. A comparative analysis between (**a**) numerical and (**b**) approximate methods, alongside (**c**) the absolute error profile and (**d**) transient time history detail.

Table 3. Quantitative verification and comparison of absolute errors between RK-4 and MTSM solutions for the controlled system (after the second mode implementation of the NDF controller).

Time	RK-4	MSM	Absolute Error
155	0.000011478	0.000011309	0.00000016867
197	−0.000065269	−0.000064720	0.00000120330
286	0.000050741	0.000049648	0.00000109280
399	0.000091589	0.000078809	0.00001278100
435	0.000073227	0.000070828	0.00000239920
521	0.000073218	0.000075251	0.00000203270
636	0.000016452	0.000018661	0.00000220860
693	−0.000052191	−0.000060261	0.00000806960
762	0.000023991	0.000019454	0.00000453700
790	−0.000078541	−0.000078767	0.00000022598
887	0.000017452	0.000018762	0.00000130970
971	−0.000073294	−0.000073529	0.00000023424

6. Bifurcation Investigation

A useful mathematical technique for examining how a dynamical system's topological or qualitative nature varies as an attribute is changed is bifurcation characterization [40]. It makes it possible to identify bifurcation locations, which are crucial places when a system's behavior drastically shifts, such as from a stable state to periodic motion or from periodic to chaotic dynamics. This kind of analysis is essential to comprehending the emergence of complicated behaviors in nonlinear systems.

On the other hand, feedback active control is essential for maintaining stability and predictable operation in nonlinear dynamical systems, as it actively counteracts bifurcations, instability, and chaos. By continuously monitoring system outputs and adjusting inputs in real time, a well-designed controller can shift critical bifurcation thresholds, suppress period-doubling routes to chaos, and prevent the system from entering unsafe parameter regions. Specifically, feedback introduces dissipation or damping that confines trajectories to a stable fixed point or limit cycle, thereby avoiding erratic, unpredictable behavior such as strange attractors. Without such control, small parametric variations or external disturbances can drive the system through bifurcation points, leading to degraded performance, mechanical fatigue, or complete loss of operational integrity. Thus, feedback control not only stabilizes the system but also ensures robust functionality under realistic, uncertain conditions. In this study, we used Poincaré maps and bifurcation diagrams for bifurcation analysis. On the other side, control tactics are used to manage and lessen chaos. By changing the system's characteristics or adding input to direct its evolution toward a desired state, these techniques stabilize the system. Predictive control, adaptive control, and NDF control—which we employed in our study—are examples of common control techniques. These methods can be used to prevent system failure, reduce chaotic oscillations, and enhance overall performance. Consequently, we talked about the presence of the controller in the dynamical model under study and how it affected the chaotic behavior of the model. To carry out our analysis, we employed a wide range of bifurcation parameters, excitation amplitudes f_1, f_2, damping coefficients μ_1, μ_2, and external excitation frequency Ω_1.

Here, we considered the damping coefficient μ_1 as a bifurcation parameter to simulate the bifurcation diagram as in Figure 28. We can observe that the system initially exhibits a dense collection of points, indicating chaotic behavior, as illustrated by the Poincaré map in Figure 28e at $\mu_1 = 0.01$,, or complex periodic motion with sensitivity to initial conditions, as illustrated by the Poincaré map in Figure 28c. By increasing the value of μ_1 near 0.2, the plot shows a dense, scattered cluster of branches, indicating a quasi-periodic behavior

or a chaotic motion, as indicated in Figure 28d,f. Figure 29 presents the bifurcation diagram and the Poincaré map for μ_2 as a bifurcation parameter. By increasing μ_2 up to 0.016, the system behaves as a chaotic motion, as shown in Figure 29c,e. Furthermore, by increasing the value of μ_2, the system behavior reached periodic doubling or quasi-periodic motion, as illustrated in Figure 29d,f, which was computed at $\mu_2 = 0.06$.. On the other hand, the increase in the parameter f_1 reaches the system from periodic to a quasi-periodic to a chaotic behavior, as described by Figure 30. The presented Poincaré map in Figure 30c,e, plotted at $f_1 = 0.5$, indicates a quasi-periodic solution for $x(t)$, and $y(t)$, where chaotic motion is described in Figure 30d,f, plotted at $f_1 = 10$. The same results were obtained for f_2 as a bifurcation parameter, which are illustrated in Figure 31. That the Poincaré map shown in Figure 31c,e is obtained at $f_2 = 0.5$, and that described in Figure 31d,f is plotted at $f_2 = 10$. In Figure 32, as the excitation frequency Ω_1 is a bifurcation parameter, the bifurcation diagram of $x(t)$ and $y(t)$ shows periodic or quasi-periodic motion unless, as the case of resonance, it reached to chaotic behavior, as shown in Figure 32a,b. Periodic or quasi-periodic motion are presented as a Poincaré map in Figure 32c,f at $\Omega_1 = 2$. Chaotic motion occurred to the second mode $y(t)$ due to the first resonance case at $\Omega_1 = 7.47$, as presented in Figure 32d,g. At $\Omega_1 = 10.77$, the first mode $x(t)$ behaved as chaotic response due to the second resonance scenario, as indicated at Figure 32e,h.

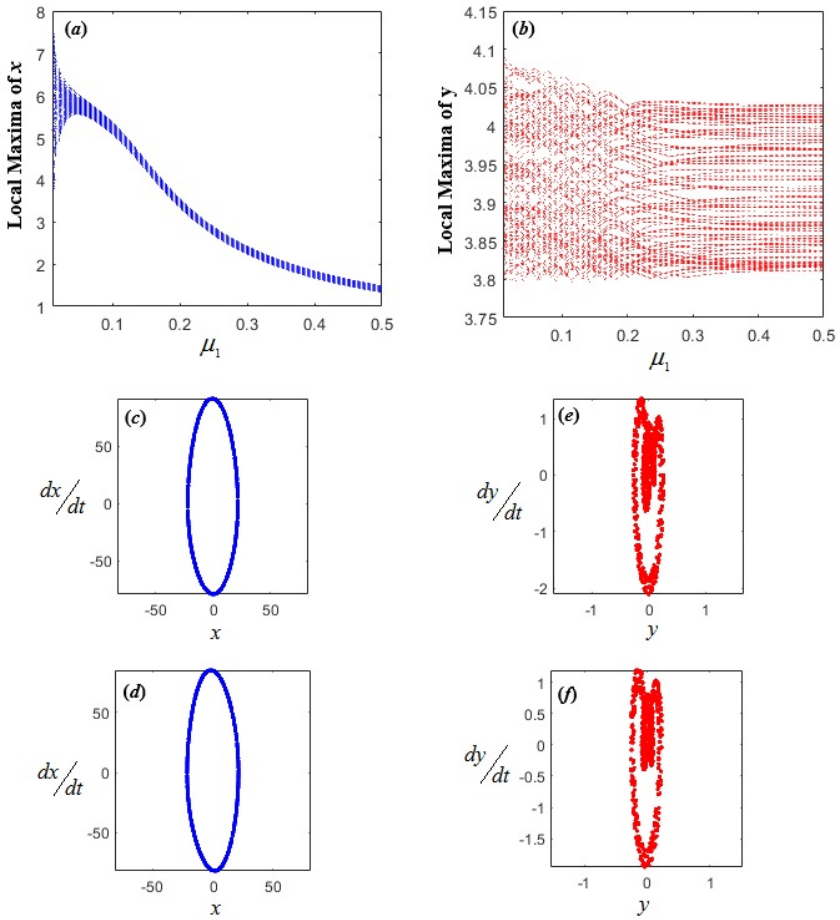

Figure 28. Bifurcation diagram and the corresponding Poincaré map versus the damping coefficient μ_1 in the case with control. (***a***) The first mode $\mu_1 - x(t)$. (***b***) The second mode $\mu_1 - y(t)$. (***c***,***e***) Poincaré map of $\mu_1 = 0.01$ and (***d***,***f***) Poincaré map of $\mu_1 = 0.2$.

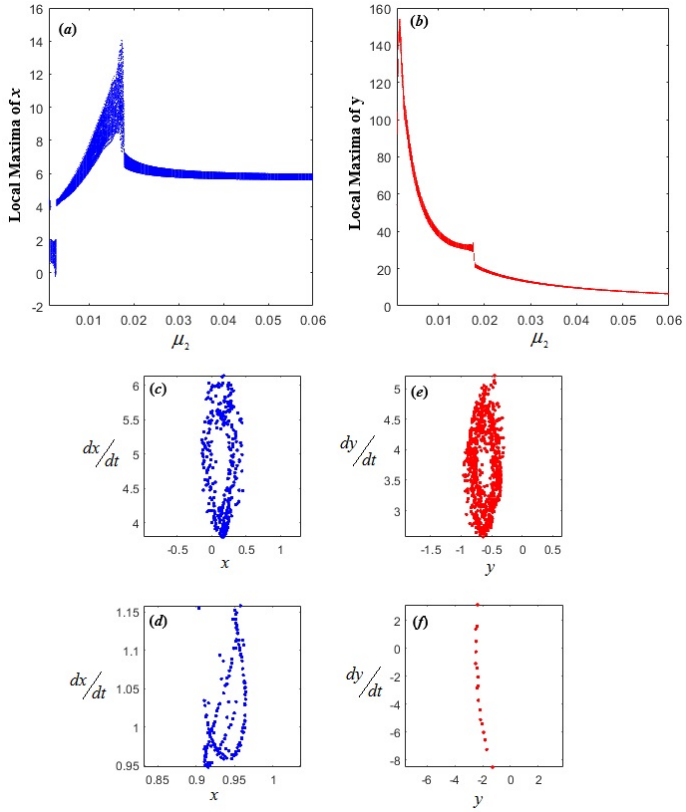

Figure 29. Bifurcation diagram and the corresponding Poincaré map versus the damping coefficient μ_2 in the case with control. (***a***) The first mode $\mu_2 - x(t)$. (***b***) The second mode $\mu_2 - y(t)$. (***c***,***e***) Poincaré map of $\mu_2 = 0.016$ and (***d***,***f***) Poincaré map of $\mu_2 = 0.06$.

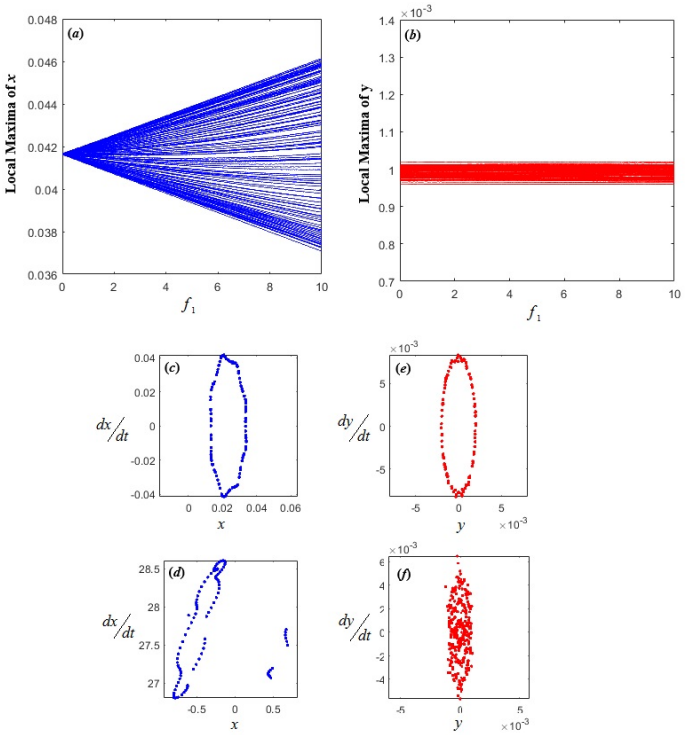

Figure 30. Bifurcation diagram and the corresponding Poincaré map versus the external force f_1 in the case with control. (***a***) The first mode $f_1 - x(t)$. (***b***) The second mode $f_1 - y(t)$. (***c***,***e***) Poincaré map of $f_1 = 0.5$ and (***d***,***f***) Poincaré map of $f_1 = 10$.

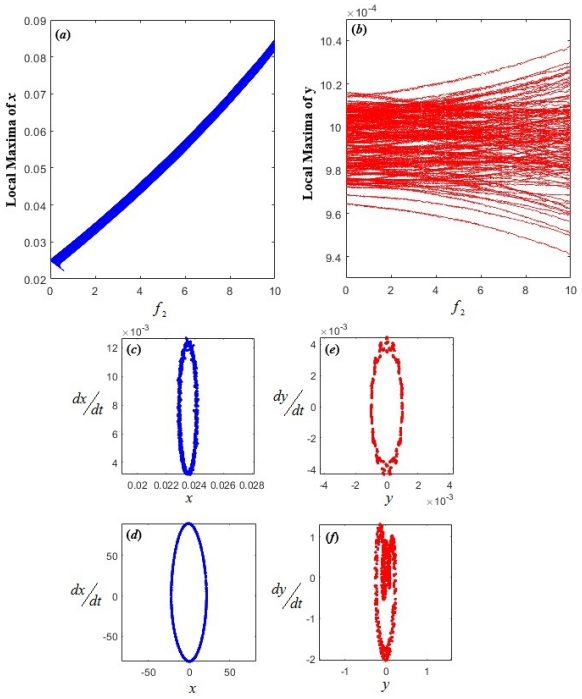

Figure 31. Bifurcation diagram and the corresponding Poincaré map versus the external force f_2 in the case with control. (***a***) The first mode $f_2 - x(t)$. (***b***) The second mode $f_2 - y(t)$. (***c***,***e***) Poincaré map of $f_2 = 0.5$ and (***d***,***f***) Poincaré map of $f_2 = 10$.

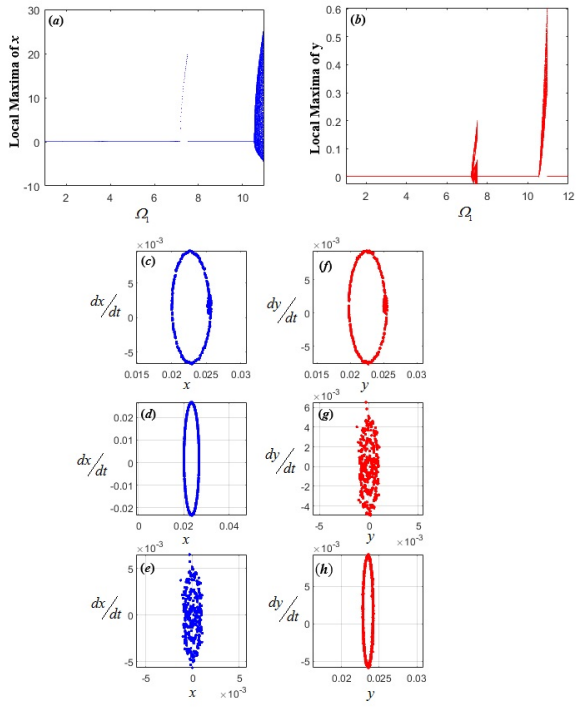

Figure 32. Bifurcation diagram and the corresponding Poincaré map versus the external frequency Ω_1 in the case with control. (***a***) The first mode $\Omega_1 - x(t)$. (***b***) The second mode $\Omega_1 - y(t)$. (***c***,***f***) Poincaré map of $\Omega_1 = 2$, (***d***,***g***) Poincaré map of $\Omega_1 = 7.47$, and (***e***,***h***) Poincaré map of $\Omega_1 = 10.77$.

7. Stability Map

The regions of parameter space where a dynamical system displays stable behavior, as identified by the eigenvalues of its linearized dynamics or by direct Lyapunov's second technique, can be seen graphically and analytically using a Lyapunov-based stability map. The hue or contour in these maps represents the sign of the biggest real part of the Lyapunov

exponents or the margin to instability, and each point represents a particular collection of system parameters (such as gains, time delays, and physical coefficients). Lyapunov-based maps, in contrast to classical bifurcation diagrams, include information about the rate of convergence or divergence, enabling scientists and engineers to differentiate between various degrees of stability (e.g., asymptotically stable vs. marginally stable) as well as between stable and unstable regions. One of the important benefits for researching dynamical systems is the parameter space design, which allows safe operating regions to be quickly identified without the need for repeated time-domain simulations. In addition, the sensitivity analysis indicates the proximity of a nominal design to instability bounds. Another benefit for researching dynamical systems is nonlinear insight, which can provide sufficient conditions for both local and global stability, not only local linear stability, when paired with Lyapunov's direct technique. Furthermore, robustness evaluation assists in measuring the permissible parameter tolerances prior to stability loss (e.g., the thickness of the stable region along each axis). Finally, the control synthesis demonstrates how Lyapunov function derivatives vary with parameters and directs adaptive control or gain scheduling. The Lyapunov-based stability map presented in Figure 33 offers a compact and insightful visualization of the system's stability landscape across the most critical parameters of the system like f_1, f_0, Ω_1, Ω_2, μ_1, and μ_2, without applying control. Figure 33a presents a systematic stability map over the parameter plane spanned by f_1 and f_0. The color-coded 'Maximum Value' serves as a proxy for the system's dynamical regime. For low f_1 values (approximately 0–0.15), with the range $0 \leq f_0 \leq 3.2$ indicating a periodic behavior, this region corresponds to stable operation (blue color). Furthermore, f_1 increasing beyond 0.15–10 suggests chaotic motion or an unstable (unsafe) region (black color). As depicted in Figure 33b, distinct unstable domains are observed for $\Omega_1 \approx$ 2–4.7 with $f_2 =$ 8–10, from $\Omega_1 \approx$ 4.9–5.2 with $f_2 =$ 0–10, and from $\Omega_1 \approx$ 5.4–8 with $f_2 =$ 6.9–10, which are represented in black. The map's ability to encode both the sign and magnitude of the Lyapunov exponent provides a quantitative margin of stability, making it superior to stable/unstable classifications. From a control engineering perspective, such maps enable the direct selection of parameter pairs that maximize the decay rate, as well as the computation of robustness radii to uncertainty in Ω_1 and f_2. The contour (μ_1, μ_2), and (Ω_1, Ω_2) present quasi-periodic and periodic motion at most spaces, as indicated in Figure 34c,d, except for $\Omega_2 \approx$ 2–8 with $\Omega_1 =$ 5.05–5.2, which gives chaotic behavior. Moreover, Figure 31 presents the stability map for the system parameters under resonance and NDF control, $k_1 = 5$, $k_2 = 5$, $k_2 = 5$, and $k_4 = 2$; this figure elucidates that the stability regions (periodic motion state) are increased by using the NDF control, which indicates the importance of the used feedback control.

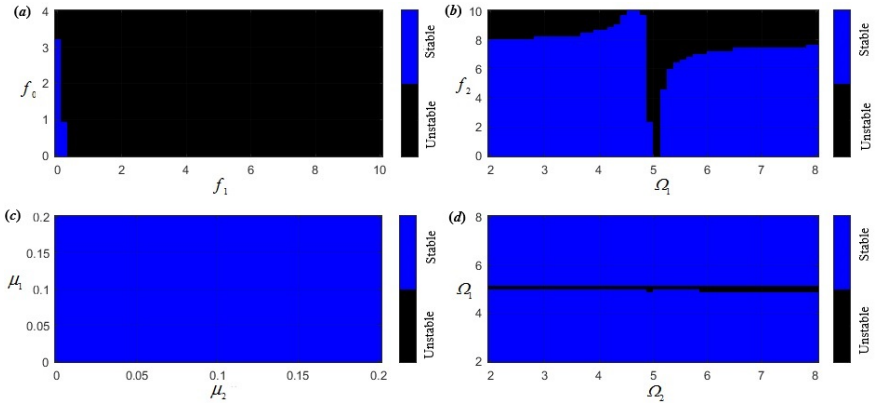

Figure 33. Lyapunov-based stability map for $k_1 = 0$, $k_2 = 0$, $k_2 = 0$, and $k_4 = 0$. (***a***) stability plane for (f_0 vs. f_1); (***b***) stability plane for (f_2 vs. Ω_1); (***c***) stability plane for (μ_1 vs. μ_2); (***d***) stability plane for (Ω_1 vs. Ω_2).

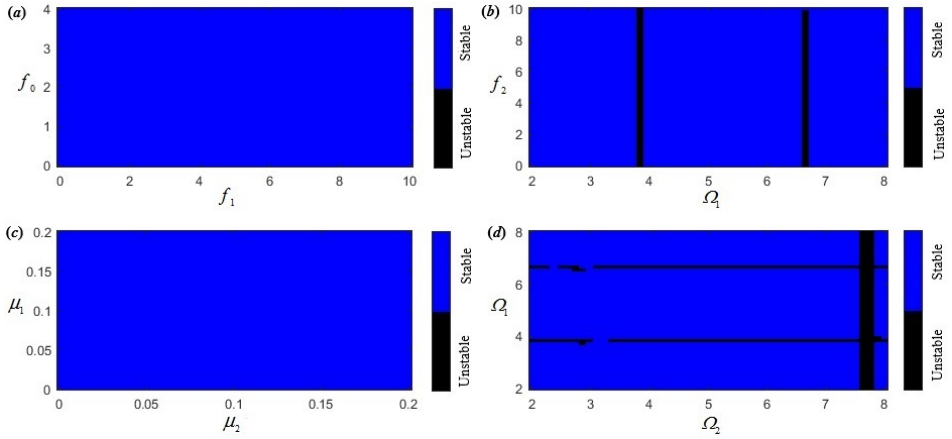

Figure 34. Lyapunov-based stability map for $k_1 = 5$, $k_2 = 5$, $k_2 = 5$, and $k_4 = 2$. (***a***) stability plane for (f_0 vs. f_1); (***b***) stability plane for (f_2 vs. Ω_1); (***c***) stability plane for (μ_1 vs. μ_2); (***d***) stability plane for (Ω_1 vs. Ω_2).

Comparison with Previous Work

Ref. [34] examines the nonlinear dynamics and stability of a coupled electromechanical oscillator under harmonic and parametric excitations. In order to validate the analytical results without using active control procedures, the study focuses on describing the system's response and parametric effects at critical resonance circumstances. In order to reduce nonlinear bifurcations and suppress vibrations in intricate electromechanical systems, this study [35] suggests a unique NPDVF controller. The suggested method shows strong stability and great energy efficiency under simultaneous resonance conditions by second-order perturbation analysis.

This work examines how well a Negative Derivative Feedback (NDF) controller suppresses vibration in a nonlinear electromechanical oscillator that is subjected to mixed excitations. The method of multiple scales (MMS) is used to develop analytical approximate solutions up to the second order, specifically for the primary resonance scenario. The system's vibration is greatly decreased after controller feedback addition, with the controller's effectiveness (E_a = amplitude without controller/amplitude with controller) approaching 590 and 51.5 for the first and second modes, respectively, according to an analysis of the time history and various parameters before and after the controller's integration. In comparison to its value without control, the vibrating system's amplitude is reduced by almost 99.8% for the first mode and 98% for the second mode. Additionally, there is a high level of agreement of analytic and approximate solutions with the maximum calculated error metric being 0.01% for the first mode and less than 10^{-5}% for the second mode across the verified parameter ranges. The bifurcation diagram, Poincaré map, and Lyapunov map are illustrated confirmed that the NDF controller maintains the required stable progression of the evolving system while reducing a chaotic state. These results demonstrate how well the controller works to enhance the dynamic functionality of the system throughout various circumstances. Additionally, the stability mapping for the system parameters was obtained and discussed to asses the optimum parameter values that ensure the system periodicity and confirming stability.

8. Conclusions

A nonlinear electromechanical system's vibrations under harmonic and parametric excitations are suppressed and eliminated using an active vibration control. The model is represented by coupled nonlinear ordinary differential equations and consists of an electrical component coupled to a mechanical component. Using the method of multiple

scales, analytical approximation solutions up to the second order are sought. The response and stability of the solutions at the worst resonance instances were examined using the time-series. The effects of various system factors were documented, and we verified the perturbation solution results using numerical simulations. Analytical and numerical simulations were compared. Furthermore, bifurcation analyses conducted for five distinct parameters (excitation amplitudes (f_1, f_2), damping coefficients (μ_1, μ_2), and external excitation frequency Ω_1)—using Poincaré maps and bifurcation diagrams—confirmed that the NDF controller maintains the required stable progression of the evolving system while reducing a chaotic state. These results demonstrate how well the controller works to enhance the dynamic functionality of the system throughout various circumstances. Additionally, the stability mapping for the system parameters was obtained and discussed to asses the optimum parameters values that ensure the system periodicity and confirming stability. The results and discussion above allow us to draw the following conclusions:

1 In nonlinear systems, the Negative Derivative Feedback (NDF) controller shows remarkable efficacy in reducing high-amplitude vibrations.
2 The controller's effectiveness (E_a = amplitude without controller/amplitude with controller) approaches 590 and 51.5 for the first and second modes, respectively.
3 Using a Negative Derivative Feedback controller reduced the vibrating system's amplitude by 99.8% and 98 % for the first and second modes compared to being deprived of control.
4 The amplitude of the primary system was monotonically decreased by the natural frequency and damping coefficients.
5 The controlled system behaved better when the external excitation force was increased.
6 The first indirect Liapunov approach was used for stability analysis in order to categorize the stable and unstable regions.
7 The numerical simulations and the analytical solutions agree quite well with the maximum calculated error metric being 0.01% for the first mode and less than 10^{-5}% for the second mode across the verified parameter ranges.
8 Optimum parameter selection was made through the system parameter effect graphs and stability mapping diagrams.
9 The chaotic response and system periodicity were demonstrated through bifurcation diagrams and Poincaré maps .

Author Contributions: A.T.E.-S.: Investigation, methodology, data curation, validation, reviewing, and editing. R.K.H.: Investigation, methodology, formal analysis, reviewing, editing, and funding acquisition. Y.A.A.: Conceptualization, resources, methodology, writing—original draft preparation, visualization, reviewing, and editing. F.S.M.: Formal analysis, validation, investigation, methodology, data curation, conceptualization, reviewing, and editing. S.A.A.: Investigation, methodology, formal analysis, reviewing, and editing. T.A.B.: Methodology, software, validation, data curation, reviewing, and editing. All authors have read and agreed to the published version of the manuscript.

Funding: This work was supported and funded by the Deanship of Scientific Research at Imam Mohammad Ibn Saud Islamic University (IMSIU) (grant number IMSIU-DDRSP2601).

Data Availability Statement: All data generated or analyzed during this study are included in this published article.

Conflicts of Interest: The authors have not revealed any conflicting interests.

List of Abbreviations and Symbols

MMS	Multiple scale method
NDF	Negative derivative feedback
PR	Primary resonance
FRCs	Frequency response curves
LNPF	Linear negative position feedback
PPF	Positive position feedback
FRE	Frequency response equation
2-DOF	Two-degree-of freedom equation
$x, \dot{x}, \ddot{x}$	Position, velocity, and acceleration of the first oscillator (mechanical part)
$y, \dot{y}, \ddot{y}$	Position, velocity, and acceleration of the second oscillator (electrical part)
$u, \dot{u}, \ddot{u}$	Position, velocity, and acceleration of the controller
$v, \dot{v}, \ddot{v}$	Position, velocity, and acceleration of the controller
$\mu_1, \mu_2, \mu_3, \mu_4$	Damping coefficients
f_1, f_2, f_3, f_4	Amplitudes of excitation force
$\omega_1, \omega_2, \omega_3, \omega_4$	Natural frequencies
$\Omega_1, \Omega_2, \Omega_3, \Omega_4$	Excitation frequencies
γ_j, β_j	Coupling terms ($j = 1, 2, 3$)
λ_1, λ_2	Nonlinear parameter
k_1, k_2, k_3, k_4	Control gains/parameters associated with the NDF controller
cc	Complex conjugate
ε	Small perturbation parameter

References

1. Okada, Y.; Matsuda, K.; Hashitani, H. Self-sensing active vibration control using the moving-coil-type actuator. *J. Vib. Acoust.* **1995**, *117*, 411–415. [CrossRef]
2. Yamapi, R.; Chabi, O.J.; Woafo, P. Harmonic oscillations, stability and chaos control in a non-linear electromechanical system. *J. Sound Vib.* **2003**, *259*, 1253–1264. [CrossRef]
3. Ge, Z.M.; Lin, T.N. Chaos, chaos control and synchronization of electro-mechanical gyrostat system. *J. Sound Vib.* **2003**, *259*, 585–603. [CrossRef]
4. Yamapi, R.; Bowong, S. Dynamics and chaos control of the self-sustained electromechanical device with and without discontinuity. *Commun. Nonlinear Sci. Numer. Simul.* **2006**, *11*, 355–375. [CrossRef]
5. Siewe Siewe, M.; Yamgoué, S.B.; Moukam Kakmeni, F.M.; Tchawoua, C. Chaos controlling self-sustained electromechanical seismograph system based on the Melnikov theory. *Nonlinear Dyn.* **2010**, *62*, 379–389. [CrossRef]
6. Yamapi, R.; Kakmeni, F.M.; Orou, J.C. Nonlinear dynamics and synchronization of coupled electromechanical systems with multiple functions. *Commun. Nonlinear Sci. Numer. Simul.* **2007**, *12*, 543–567. [CrossRef]
7. Yamapi, R.; Aziz-Alaoui, M.A. Vibration analysis and bifurcations in the self-sustained electromechanical system with multiple functions. *Commun. Nonlinear Sci. Numer. Simul.* **2007**, *12*, 1534–1549. [CrossRef]
8. Kwuimy, C.K.; Woafo, P. Dynamics of a self-sustained electromechanical system with flexible arm and cubic coupling. *Commun. Nonlinear Sci. Numer. Simul.* **2007**, *12*, 1504–1517. [CrossRef]
9. Kitio Kwuimy, C.A.; Woafo, P. Dynamics, chaos and synchronization of self-sustained electromechanical systems with clamped-free flexible arm. *Nonlinear Dyn.* **2008**, *53*, 201–213.
10. Hegazy, U.H. Dynamics and control of a self-sustained electromechanical seismographs with time-varying stiffness. *Meccanica* **2009**, *44*, 355–368.
11. Martens, W.; von Wagner, U.; Litak, G. Stationary response of nonlinear magneto-piezoelectric energy harvester systems under stochastic excitation. *Eur. Phys. J. Spec. Top.* **2013**, *222*, 1665–1673. [CrossRef]
12. Borowiec, M.; Litak, G.; Lenci, S. Noise effected energy harvesting in a beam with stopper. *Int. J. Struct. Stab. Dyn.* **2014**, *14*, 1440020. [CrossRef]
13. Xu, M.; Jin, X.; Wang, Y.; Huang, Z. Stochastic averaging for nonlinear vibration energy harvesting system. *Nonlinear Dyn.* **2014**, *78*, 1451–1459. [CrossRef]
14. Li, H.; Qin, W.; Lan, C.; Deng, W.; Zhou, Z. Dynamics and coherence resonance of tri-stable energy harvesting system. *Smart Mater. Struct.* **2016**, *25*, 015001.

15. Pallay, M.; Daeichin, M.; Towfighian, S. Feasibility study of a micro-electro-mechanical-systems threshold-pressure sensor based on parametric resonance: Experimental and theoretical investigations. *J. Micromech. Microeng.* **2021**, *31*, 025002.
16. Yang, Y.; Liu, C.; Chen, L.; Zhang, X. Phase deviation of semi-active suspension control and its compensation with inertial suspension. *Acta Mech. Sin.* **2024**, *40*, 523367. [CrossRef]
17. Mao, X.Y.; Ding, H.; Chen, L.Q. Parametric resonance of a translating beam with pulsating axial speed in the super-critical regime. *Mech. Res. Commun.* **2016**, *76*, 72–77. [CrossRef]
18. Siewe, M.S.; Tchawoua, C.; Rajasekar, S. Parametric resonance in the Rayleigh–Duffing oscillator with time-delayed feedback. *Commun. Nonlinear Sci. Numer. Simul.* **2012**, *17*, 4485–4493. [CrossRef]
19. Aghamohammadi, M.; Sorokin, V.; Mace, B. On the response attainable in nonlinear parametrically excited systems. *Appl. Phys. Lett.* **2019**, *115*, 154102. [CrossRef]
20. Chen, S.; Epureanu, B. Forecasting bifurcations in parametrically excited systems. *Nonlinear Dyn.* **2018**, *91*, 443–457.
21. Warminski, J. Nonlinear dynamics of self-, parametric, and externally excited oscillator with time delay: Van der Pol versus Rayleigh models. *Nonlinear Dyn.* **2020**, *99*, 35–56.
22. Li, D.; Shaw, S.W. The effects of nonlinear damping on degenerate parametric amplification. *Nonlinear Dyn.* **2020**, *102*, 2433–2452. [CrossRef]
23. Nayfeh, A.H.; Mook, D.T. *Nonlinear Oscillations*; John Wiley & Sons: Hoboken, NJ, USA, 2024.
24. Hu, M.; Zeng, Y.; Li, D.; Luo, H.; Wei, J.; Liu, K. 4-DOF Full-Speed Range Vibration Suppression of an Active–Passive Supported Flywheel Rotor Based on Inverse System Decoupling. *Actuators* **2026**, *15*, 157. [CrossRef]
25. Ozsoy, M.; Sims, N.D.; Ozturk, E. Actuator saturation during active vibration control of milling. *Mech. Syst. Signal Process.* **2025**, *224*, 111942. [CrossRef]
26. Su, Z.; Cui, Z.; Huang, H. Primary resonance suppression in spur gear systems using hybrid proportional and fractional-order derivative displacement feedback control. *Aims Math.* **2026**, *11*, 1857–1877. [CrossRef]
27. Bauomy, H.S. Active control impact analysis on shaped coupled beam structure. *Aims Math.* **2025**, *10*, 3073 [CrossRef]
28. Saeed, N.A.; Elashmawey, R.A.; Nassar, M.E.; Hou, L.; Zhong, S.; Duraihem, F.Z. Three control techniques for suppressing nonlinear vibrations in a 2-DOF dynamical system subjected to combined external and multi-parametric harmonic excitations with 1: 1 internal resonance. *J. Low Freq. Noise Vib. Act. Control* **2025**, *44*, 2363–2406. [CrossRef]
29. Yang, M.; Lou, J.; Yang, Q.; Chu, J.; Chai, K.; Tan, M.; Lin, T. Vibration Suppression and Bifurcation Analysis of a Two-DOF Structure Coupled with PMNES. *Aerospace* **2026**, *13*, 123. [CrossRef]
30. EL-Sayed, A.T.; Hussein, R.K.; Amer, Y.A.; EL-Sayed, M.A. Stability Enhancement and Bifurcation Mitigation in Nonlinear Inner Plate Oscillations Through PD Control. *Machines* **2025**, *13*, 828. [CrossRef]
31. El-Sayed, A.T.; Bauomy, H.S.; Amer, T.S.; Abohamer, M.K. Stability and Bifurcation Effects in Nonlinear Vibratory Systems Under NIPPF Control. *J. Vib. Eng. Technol.* **2026**, *14*, 45. [CrossRef]
32. EL-Sayed, A.T.; Alanazy, A.; Amer, Y.A.; EL-Sayed, M.A. Effect of geometrically nonlinear damping on systems controlled by negative derivative feedback under harmonic excitation. *J. Low Freq. Noise Vib. Act. Control* **2025**, *44*, 2222–2241. [CrossRef]
33. Alanazy, A.; Amer, Y.A.; EL-Sayed, A.T.; Mohammed, F.S.; Bahnasy, T.A. Multi-Control Strategies on a Cubic–Quintic Nonlinear Hybrid Oscillator with External Excitation Under Resonance Conditions. *Mathematics* **2025**, *13*, 957. [CrossRef]
34. Hamed, Y.S.; Sayed, M.; Alshehri, A.A. Active vibration suppression of a nonlinear electromechanical oscillator system with simultaneous resonance. *J. Vibroeng.* **2018**, *20*, 42–61. [CrossRef]
35. Bauomy, H. Control and optimization mechanism of an electromagnetic transducer model with nonlinear magnetic coupling. *Aims Math.* **2025**, *10*, 2891–2929. [CrossRef]
36. Kevorkian, J.; Cole, J.D. The method of multiple scales for ordinary differential equations. In *Multiple Scale and Singular Perturbation Methods*; Springer: New York, NY, USA, 1996; pp. 267–409.
37. Xu, Y.; Jiao, Y.; Chen, Z. Recent Advances in Nonlinear Dynamics Applied in Electromechanical Systems. *Appl. Sci.* **2025**, *15*, 12908. [CrossRef]
38. Puzyrov, V.; Losyeva, N.; Savchenko, N.; Termenzhy, D. The negative derivative feedback controller tuning for vibration suppression. In *Advances in Machinery, Materials Science and Engineering Application XI: Proceedings of the 11th International Conference (MMSE 2025)*; SAGE Publications: Paris, France, 2025; pp. 561–567.
39. Dukkipati, R.V. *Solving Vibration Analysis Problems Using Matlab*; New Age International Pvt Ltd Publishers: New Delhi, India, 2007.
40. Amer, Y.A.; Bahnasy, T.A.B.A.; Elmhalawy, A.M. vibration control for a coupled pitch-roll ship model via a negative cubic velocity feedback control. *J. Eng. Res.* **2021**, *5*, 31–38.

Disclaimer/Publisher's Note: The statements, opinions and data contained in all publications are solely those of the individual author(s) and contributor(s) and not of MDPI and/or the editor(s). MDPI and/or the editor(s) disclaim responsibility for any injury to people or property resulting from any ideas, methods, instructions or products referred to in the content.